University of California
Santa Barbara

Studying Energy Loss Mechanisms in MEMS Based Contour-Mode Resonators Using Laser Doppler Vibrometery

A dissertation submitted in partial satisfaction
of the requirements for the degree

Doctor of Philosophy
in
Mechanical Engineering

by

Brian A. Gibson

Committee in charge:

Professor Kimberly L. Turner, Chair
Professor Ania Bleszynski Jayich
Professor Jeff Moehlis
Professor Brad Paden

December 2016

The Dissertation of Brian A. Gibson is approved.

Ania Bleszynski Jayich

Jeff Moehlis

Brad Paden

Kimberly L. Turner, Committee Chair

December 2016

Studying Energy Loss Mechanisms in MEMS Based Contour-Mode Resonators Using Laser Doppler Vibrometery

by

Brian A. Gibson

This is dedicated to my wife, Karen, and my children, Jack, Jane, and Kate.

Acknowledgements

I want to thank my advisor, Professor Kimberly Turner. Her guidance and support were unparalleled and I could not have made it through if it was not for her compassion and understanding. She went above and beyond what is necessary of a PhD. advisor. I would also like to thank my other committee members, Professor Ania Bleszynski Jayich, Professor Jeff Moehlis and Professor Brad Paden. It is very humbling to be supported by such talented people.

I would like to thank my lab partners, Lily Li, Kamala Qalandar, Jamie Booth, and Luke Patterson. Their help and humor is what defined my graduate experience. I would also like to thank past TurnerMEMS students including Chris Burgner, Kari Moran, John Tamelier and Sathya Chary. Dave Bothman deserves a special thanks as well. The lab would not be functioning if it wasn't for his constant assistance.

The people at Carnegie-Mellon University, under the guidance of Professor Gianluca Piazza were our colleagues on this project and provided knowledge and devices that were essential to my work. Cristian Cassella and Jeronimo Segovia-Fernandez provided tremendous support in the area of electrical engineering and I am very grateful.

Thank you to my parents, Joe and Gretchen and my in-laws, Jack and Jan Nylund. I could not have done it without all of your support. I want to thank my kids, Jane, Kate and Jack. Through some of the tough times, their laughs and the thought of them having two doctors for parents were the only things that kept me going. I want them to know that if I can do it so can you.

Most importantly I want to thank my wife, Professor Karen Nylund-Gibson. She is a shining example of a professional parent. It is only because of her that the thought of going back to school was even a possibility, let alone graduate school. She made it happen and I never would have dreamed of getting a PhD. before meeting her.

This work was supported by DARPA DEFYS program grants #8-442550-59085-FKGKT11-2.

Curriculum Vitæ

Brian A. Gibson

Education

2016	Ph.D. in Mechanical Engineering (Expected), University of California, Santa Barbara.
2011	B.S. in Mechanical Engineering, University of California, Santa Barbara.
1997	B.A. in Film and Electronic Arts, California State University, Long Beach.

Experience

2016	Student Engineering Mentor, Dos Pueblos Engineering Academy
2015-2016	Teaching Assistant, Capstone Engineering Design (ME189A,B,C)
2014-2015	Teaching Assistant, Capstone Engineering Design (ME189A,B,C)
2014-2015	Teaching Assistant, Mechanical Engineering Design (ME156A,B)
2013	SABRE Program Summer Research Mentor
2012	INSET Program Summer Research Mentor
2011-2012	Internship, Owl Biomedical
2011-2012	Teaching Assistant, Introduction to Machine Shop (ME12S)
2009	INSET Summer Internship, UC Santa Barbara
1997-2009	Camera Technician, Film Industry, Los Angeles

Publications

Gibson, Brian, K. R. Qalandar, G. Piazza, and K. Turner, "A Novel Method for Measuring Ring-Down In a High Noise and High Frequency System Using Laser Doppler Vibrometery" in *Proceedings of Solid State Sensors, Actuators, and Microsystems Workshop*, Hilton Head (2016), pp. 293294.

Gibson, B., Qalandar, K., Turner, K., Cassella, C., & Piazza, G. (2015, April). Analysis of the impact of release area on the quality factor of contour-mode resonators by laser Doppler vibrometry. In *2015 Joint Conference of the IEEE International Frequency Control Symposium & the European Frequency and Time Forum* (pp. 709-712). IEEE.

Qalandar, K. R., Strachan, B. S., Gibson, B., Sharma, M., Ma, A., Shaw, S. W., & Turner, K. L. (2014). Frequency division using a micromechanical resonance cascade. *Applied Physics Letters*, 105(24), 244103.

B. S. Strachan, K. R. Qalandar, B. Gibson, M. Sharma, S. W. Shaw, and K. Turner, A Passive Micromechanical Frequency Divider. in *Proceedings of Solid State Sensors, Actuators, and Microsystems Workshop*, Hilton Head (2014), pp. 293294.

Ng, E. J., Yang, Y., Hong, V. A., Ahn, C. H., Christensen, D. L., Gibson, B. A., ... & Kenny, T. W. (2014, January). Stable pull-in electrodes for narrow gap actuation. In *2014 IEEE 27th International Conference on Micro Electro Mechanical Systems (MEMS)* (pp. 1281-1284). IEEE.

Piazza, G., Tazzoli, A., Miller, N., Segovia, J., Cassella, C., Koo, J., ... & Palmer, T. (2013, July). Dynamics of microscale thin film AlN piezoelectric resonators enables low phase noise UHF frequency sources. In *European Frequency and Time Forum & International Frequency Control Symposium (EFTF/IFC)*, 2013 Joint (pp. 555-558). IEEE.

Presentations

"A Novel Method for Measuring Ring-Down in a High Noise and High Frequency System Using Laser Doppler Vibrometry", with K. Qalandar, G. Piazza, and K.L. Turner. Poster Presentation. At: Solid State Sensors, Actuators, and Microsystems Workshop, Hilton Head (2016)

"Analysis of the Impact of Release Area on the Quality Factor of Contour-Mode Resonators by Laser Doppler Vibrometry", with K. Qalandar, C. Cassela, G. Piazza, and K.L. Turner. Conference Talk. At: IEEE International Frequency Control Symposium, Denver, CO (2015)

"Finite Element Model Verification of High Frequency Piezoelectric Contour-Mode MEMS Resonators Using Laser Doppler Vibrometry", with K.R. Qalandar, L.A. Shaw, S.Y. Chiu, A. Tazzoli, J. Segovia, M. Rinaldi, G. Piazza, and K.L. Turner. Poster Presentation. At: 60th Annual Advanced Vacuum Society International Symposium and Exhibition, Long Beach, CA (2013).

Awards

2015	Outstanding Teaching Assistant of the Year
2015	Ralph M. Parsons Foundation Graduate Student Fellowship

2014	Department of Mechanical Engineering Excellence Fellowship
2010	Member, Tau Beta Pi, Engineering Honor Society
2009	Dean's List, UCSB
2009	Lauri Converse Memorial Scholarship
2008	National Engineer's Week Scholarship

Abstract

Studying Energy Loss Mechanisms in MEMS Based Contour-Mode Resonators Using Laser Doppler Vibrometery

by

Brian A. Gibson

The work in this thesis aims to uncover energy loss mechanisms in MEMS-based piezoelectric contour-mode resonators. Quality factors for these devices has been constrained to under 10,000, limiting their commercial applications. The first part of this thesis studies Q degredation related to anchor losses. During fabrication, the outer edge of the anchors are released from the substrate due to an isotropic etch step used in releasing the device from the substrate. This allows both ends of the anchors and the surrounding region of the device layers to undergo strain resulting in energy loss during operation. This study finds that a variation in Q of up to 31% can occur as a result of this released area. A novel method for minimizing this loss through modified boundary conditions is also analyzed and experimentally tested.

The second part of this thesis develops a new method of measuring ring-downs at ultra high frequencies using laser Doppler vibrometry. Due to an inherently low signal to noise ratio and a 4ns timing error in the vibrometer measurement triggering, traditional ring-down methods are not possible at ultra high frequencies. The method outlined here overcomes this and produces results with an error of less than 6% when compared to electrically determined values.

Next, a method is outlined for measuring the magnitudes of the individual material wavelengths on the surface of the resonator. The devices are composed of multiple material layers, each with a unique acoustic velocity. As a result, at resonance, each

layer has a unique wavelength that can be measured using laser Doppler vibrometery.

The final section combines the previous two methods to measure the ring-downs of the individual material layers used in the construction of the resonators. Due to their unique material properties, the rate at which the vibrations of each material decays can be quantified to determine future fabrication choices.

Contents

List of Figures

List of Tables

Chapter 1

Introduction

The demand for consumer wireless devices continues to grow exponentially. By the end of 2015 there were 378 million wireless devices in use in the U.S. alone totaling $192 billion in sales [1]. According to the Cellular Telephone Industries Association (CTIA), 48.3% of U.S. households use mobile phones exclusively for voice calls. In addition, there will be in excess of 16 billion Wi-Fi enabled devices shipped worldwide by the end of 2016 [2].

With this demand comes an equivalent demand for smaller and more efficient devices. The unique qualities of MEMS resonators places them in a position to fulfill this demand. As opposed to traditional crystal resonators, devices such as those described in [3, 4, 5, 6, 7, 8, 9, 10, 11, 12] are CMOS compatible, allowing them to be fabricated onto the same chip as the associated electronics. This integration allows for a substantial reduction in size and weight over current resonators.

Figure 1.1 shows a schematic of a typical super-heterodyne transceiver used in RF communications. Multiple resonators, currently in the form of surface acoustic wave (SAW) filters and temperature controlled crystal oscillators (TCXO) are used in these circuits. The TCXO crystal is a discreet component that must be placed onto the chip

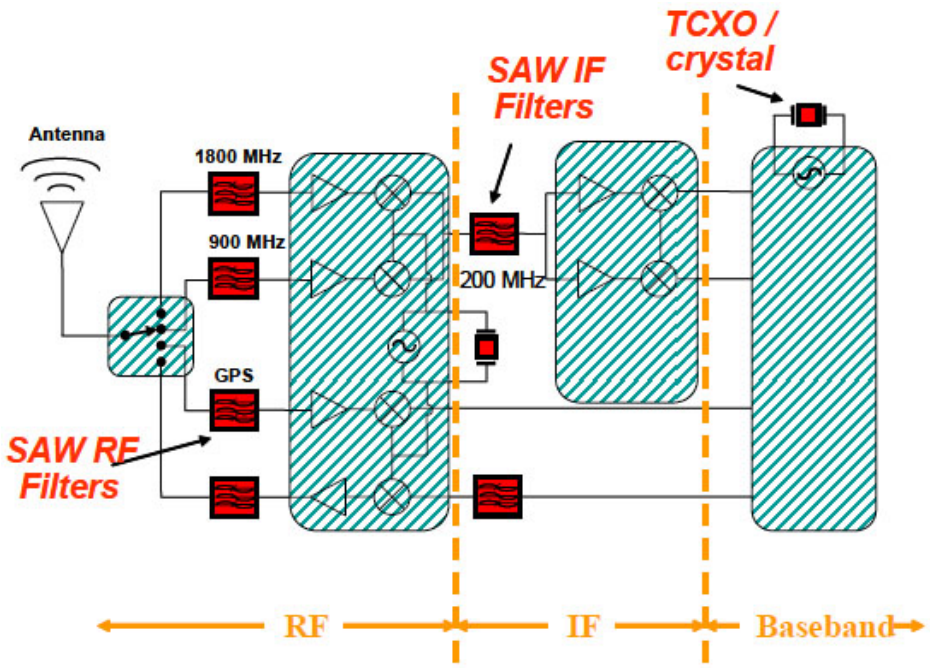

..

Figure 1.1: A Schematic of a Super Heterodyne Transceiver used in front-end wireless technology. The SAW filters and TCXO crystal (in red) are external, non-CMOS compatible components. Image courtesy of Prof. Gianluca Piazza

after fabrication which is costly, time consuming and bulky. The SAW filters are also very bulky and require specific and carefully controlled device layer thicknesses that make it impossible to integrate as on-chip devices due to the multiple frequencies necessary for such a circuit.

Piezoelectric contour-mode resonators (CMRs) have shown great promise due to their high electro-mechanical coupling coefficients, their ability to reach frequencies in excess of 2 GHz and the ability to set their frequency in CAD, allowing multiple device frequencies to be fabricated on the same chip [8, 9]. One of the limiting factors for the integration of CMRs is their relatively low quality factors. Quality factors as high as 4000 have been reached [13, 14] which is an order of magnitude lower than traditional quartz crystal-based resonators. This thesis investigates energy loss mechanisms in aluminum nitride (AlN) CMRs through the use of laser Doppler vibrometery (LDV).

1.1 Thesis Outline

This thesis can be divided into three parts: background information, an anchor loss study, and ring-down measurements. Chapter 2 provides background information on resonator applications and how resonators work as well as key characterization parameters. It also provides information on the design and fabrication of the aluminum nitride CMRs used in this thesis. Finally, it includes energy loss mechanisms present in resonators including anchor loss, interfacial loss, viscous damping, and thermoelastic dissipation.

Chapter 3 studies the effect of the released substrate regions on Q. When fabricating aluminum nitride CMRs the isotropic etch step that releases the body of the resonator from the substrate also releases a large region outside of the support anchors. This allows both sides of the anchor to undergo motion that results in substantial energy loss into the substrate region. As will be shown, this can cause a loss in quality factor of up to 31%.

Chapter 4 details a new method for measuring ring-downs using LDV. This method overcomes the limitations inherent in an ultra high frequency LDV system due to triggering error and a low signal to noise ratio. Effective measurements were taken at initial displacements as low as $1 \times 10^{-12} m$. The measurements taken with the LDV match the electrically determined measurements with an error of less than 6%. This method is applied to 220MHz AlN CMRs but could be extended to higher frequencies and to other resonant devices.

Chapter 5 describes a method for measuring the multiple wavelengths present on the surface of a CMR during operation. Because a CMR is composed of multiple material layers, each with unique acoustic velocities, the mode shape on the surface of the resonator is a superposition multiple wavelengths. This mode shape is detectable exclusively through LDV measurements, which provides the ability to measure the magnitudes of

each of these wavelengths.

Chapter 6 combines the previous two chapters to measure the ring-down of each material layer of the CMR. A method is described to measure the ring-down of the mode shape of the surface of the resonator. By studying how each wavelength decays within the mode shape during the ring-down, it is possible to determine energy loss values for each of the materials in the CMR.

Chapter 2

Background

2.1 What is a resonator?

Within every wireless device, there is an oscillator circuit (figure 2.1). The role of an oscillator is to produce an oscillating voltage that is then used to send and receive the electromagnetic signals. Within an oscillator circuit, a key component is the resonator. This component sets the frequency of oscillation of this circuit. Whether through a flexural or bulk acoustic mode, the physical vibrations of this component are transduced into an electric signal which is then amplified and fed back into the resonator for sustained oscillations. The resonator acts like a very narrow bandpass filter (figure 2.2), allowing only a very narrow range of frequencies to pass through. In doing so, the oscillator circuit produces a sinusoidal voltage at a very specific frequency that is set by the resonator. The term oscillator and resonator are often used interchangeably but for the purposes of this thesis an oscillator is a complete system including the resonator and the feedback circuit whereas the resonator is just the vibrating piezoelectric device that sets the frequency of oscillation.

As described in the introduction, resonators also serve in filter banks in radio front-

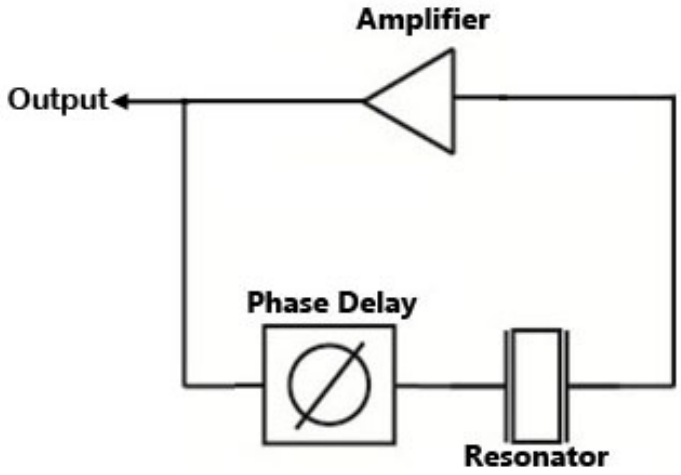

..

Figure 2.1: A schematic of a simple oscillator circuit. The resonator serves to set the operating frequency.

ends. After the wireless signal is received by the antenna, the resonator suppresses all undesired frequencies. The narrow bandwidth of the resonator is necessary to keep neighboring frequencies from being received and causing interference. To this end, a resonator with a higher quality factor will result in a wireless device with higher performance.

2.1.1 Characterization of Resonators

A key figure of merit for resonator performance is the quality factor, Q. This is an inverse measure of the energy dissipation per cycle of the resonator

$$Q = 2\pi \frac{E_{st}}{E_{dis}} \tag{2.1}$$

where E_{st} is the energy stored in the resonator and E_{dis} is the energy that is dissipated by the resonator per cycle. High quality factors are important in resonator design in order to minimize oscillator phase noise and power consumption [15]. Appendix C provides

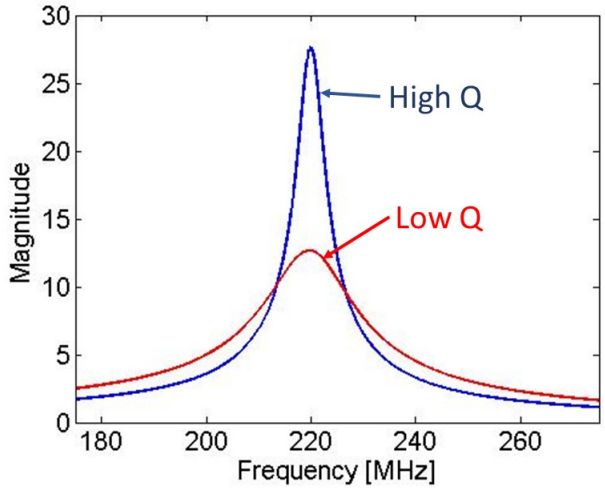

..

Figure 2.2: Two examples of typical frequency responses of a resonant device. A resonator is effectively a very narrow bandpass filter. The quality factor, Q, of the resonator defines the efficiency of the device as well as the its bandwidth. The low Q device has a wider bandwidth than the high Q device.

detail phase noise and the effects of Q. Sections 2.4-2.7 will elaborate on sources of Q degradation. High quality commercial quartz resonators can reach quality factors as high as 3 million. The typical method for determining Q is through analysis of electrical admittance data on a vector network analyzer which is described in Appendix D. Quality factor also provides a figure of merit for the frequency selectivity of the resonator. As shown in figure 2.2, a device with a higher Q has a bandwidth that is narrower than a low Q device.

Another measure for the performance of a resonator is its electro-mechanical coupling coefficient, K_t^2. This parameter defines the devices efficiency in transducing an electrical signal into mechanical motion [16]

$$K_t^2 = \frac{E_{mech}}{E_{total}} \times 100\% = \frac{1}{1 + \frac{Eelec}{E_{mech}}} \times 100\% \tag{2.2}$$

where E_{mech} is the mechanical energy stored in the device, E_{elec} is the electrical energy

stored in the device and $E_{total} = E_{mech} + E_{elec}$. The value for K_t^2 is the percentage of total energy in the device that has been converted to mechanical energy. Typical values for K_t^2 range from 0.3-6% for contour-mode resonators [17] to 17% for electro-statically driven flexural resonators. This measurement can also be determined by analyzing admittance data as described in Appendix D.

2.2 AlN CMR Design and Fabrication

The resonators studied in this thesis are aluminum nitride (AlN) based contour-mode resonators (CMR) [18],[9],[19]. They are piezoelectric devices consisting of an AlN device layer sandwiched on the top and bottom by two metal electrode layers (figure 2.3). The top electrode layer consists of interdigitated electrodes and the bottom metal layer is a solid, floating electrode used to contain the electromagnetic field. By applying an AC voltage to the electrodes at the device's resonant frequency, in-plane Lamb waves develop as a result of the strain induced by the d_{31} piezo-electric coefficient in the AlN. The operating frequency is set by [9]

$$f_0 = \frac{1}{2W}\sqrt{\frac{E_{eq}}{\rho_{eq}}} \tag{2.3}$$

where W is the electrode spacing, and E_{eq} and ρ_{eq} are the equivalent Young's modulus and density, respectively, of the combined three layers. The equivalent Young's modulus is a result of the combined contribution of each layer's stiffness proportional to its thickness,

$$E_{eq} = \frac{\sum_{i=1}^{n} E_i l_i}{\sum_{i=1}^{n} l_i} \tag{2.4}$$

where E is the Young's modulus of each material and l is the thickness of the material. The equivalent density, ρ_{eq} can be found in a similar manner.

$$\rho_{eq} = \frac{\sum_{i=1}^{n} \rho_i l_i}{\sum_{i=1}^{n} l_i} \tag{2.5}$$

Because the frequency of a CMR is set by the electrode spacing and not the thickness

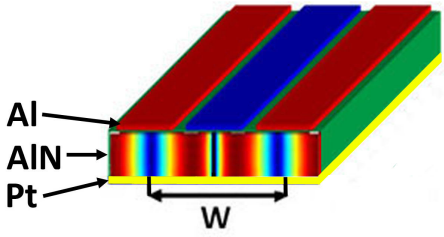

..

Figure 2.3: A schematic of the aluminum nitride piezo-electric resonators. The frequency is set by the spacing of the electrodes.

of the piezo-electric layer, as in film bulk acoustic resonators (FBARs) [20], multiple resonators with different frequencies can be lithographically patterned onto the same substrate allowing greater design flexibility. The fabrication process is also CMOS compatible allowing the resonator to be manufactured directly on-chip.

The fabrication sequence is shown in figure 2.4. A 10nm layer of titanium was deposited onto a silicon substrate to provide effective adhesion for the next layer, 100nm of platinum to form the bottom electrode (a). Two different aluminum nitride thicknesses were deposited for this thesis. Devices with a $1\mu m$ AlN layer were used as well as devices with a $1.5\mu m$ AlN thick layer. The aluminum nitride layer was sputtered on using an aluminum target in the presence of a N_2/Ar atmosphere (b). Careful control over the chamber pressure as well as the voltage of the RF power must be maintained to ensure low residual stress and high c-axis orientation [21, 22]. A 100nm of metal was then patterned to form the top electrode layer (c). A Cl_2-based dry etch was used to form the device shape by etching the aluminum nitride (d). The final step used an isotropic XeF_2

dry etch to release the device from the substrate (e). Figure 2.5 shows a microscope

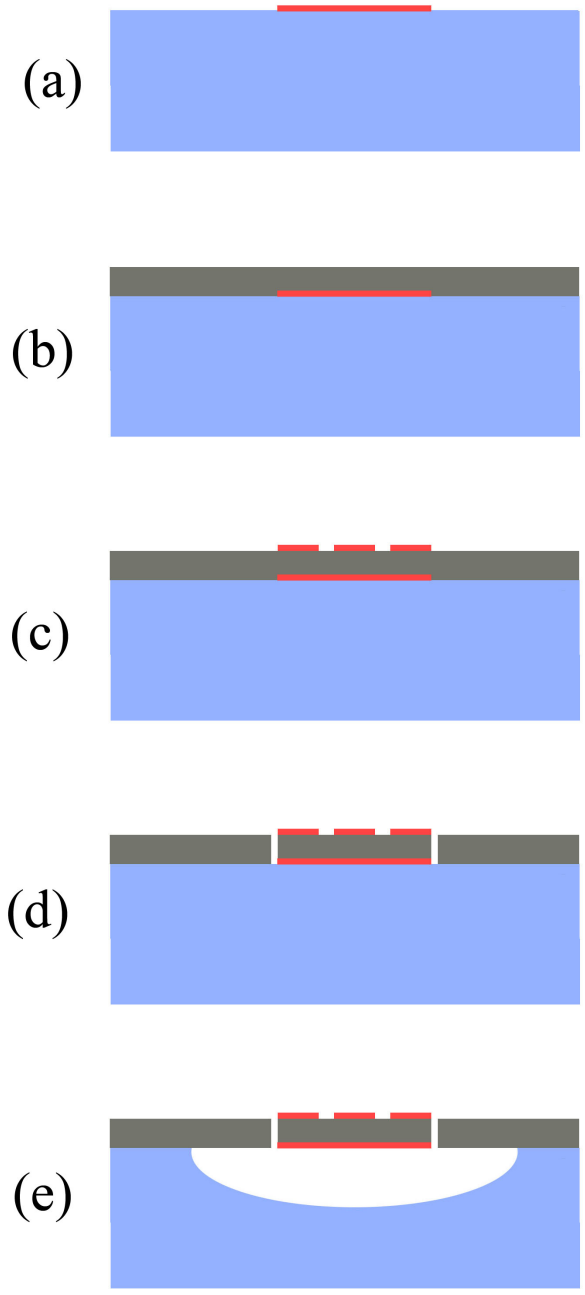

..

Figure 2.4: The fabrication sequence for the AlN contour-mode resonators. A 10nm layer of Ti is deposited onto an Si substrate followed by 100nm of Pt (a). AlN is then sputtered on (b) followed by 100nm of Al (C). The AlN layer is patterned using a Cl_2 dry etch (d). The last step uses XeF_2 to etch the Si and release the device from the substrate (e).

image of a 220MHz CMR. The area extending from the tip of the center electrode on the right to the tips of the outer electrodes on the left defines the active region of the device where the acoustic energy is generated and transduced. The bus bars in the inactive region are necessary to distribute the electrical current to the electrodes and the anchors suspend the body of the resonator above the substrate.

Figure 2.5 also shows an undesired side effect of the isotropic XeF_2 etch process. The purpose of this etch is to release the body and anchors of the resonator from the substrate but it also undercuts the region of the device layer outside of the anchors. This can be seen as a dark brown area in the figure. Because it is released from the substrate, this region is capable of motion as a result of the acoustic energy transmitted through the anchors from the active region. If this is not properly designed, energy can be lost to the substrate and result in a lower Q. This is the subject of Chapter 3.

For this study, two different aluminum nitride thicknesses were used; $1\mu m$ and 1.5 μm. A study was conducted [22] using a $5.9\mu m$ thick AlN layer at 720 and 800MHz. Using somewhat different electrode configurations, the devices in the study were called Two-Dimensional-mode Resonators that coupled in and out-of-plane modes to enhance K_t^2 values up to 3.4%. Because this design couples the in-plane and-out-of-plane modes, the thickness of the AlN layer must change depending on the desired operating frequency. This limits the number of different resonator frequencies that can be fabricated on a single chip and therefore reduces its utility in future commercial designs.

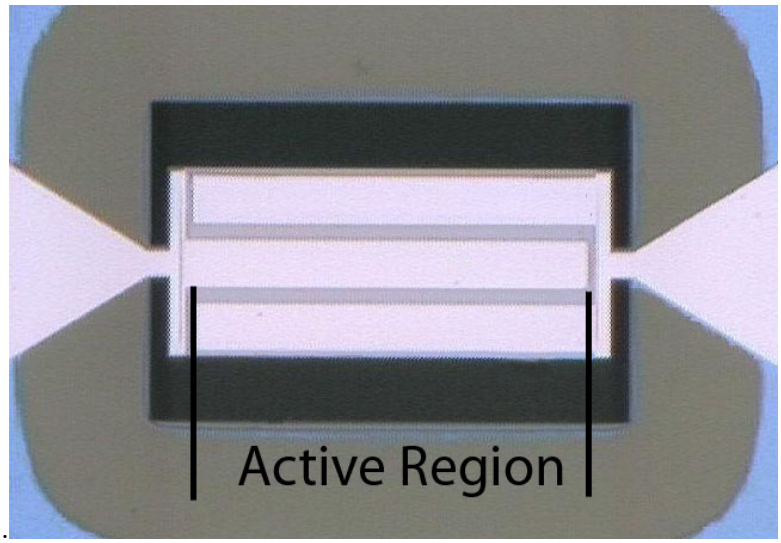

Figure 2.5: A microscope image of a 220MHz CMR. The area covered by the electrodes defines the active region of the device where the acoustic energy is transduced. The inactive region is necessary for power distribution and physical support.

2.3 Energy Loss Mechanisms in CMRs

The overall energy loss per cycle in a resonator is the result of many difference mechanisms. Each of these can have an associated quality factor that sum as

$$\frac{1}{Q_{total}} = \frac{1}{Q_{anchor}} + \frac{1}{Q_{interfacial}} + \frac{1}{Q_{TED}} + \frac{1}{Q_{viscous}} + ... \tag{2.6}$$

The most common and dominate energy loss mechanisms for contour-mode resonators are given below. This thesis focuses on anchor losses and interfacial losses.

2.4 Anchor Loss

Anchor loss is the result of the scattering of acoustic waves originating in the body of the resonator into the substrate [23]. In [19] it was shown that, at frequencies below 370MHz, anchor loss has a greater effect on Q than interfacial losses or any other mechanism. The study tested devices operating at 220MHz, 370MHz, and 1.05GHz. Through

experimental measurements it was shown that the length, L_a (figure 2.6), of the support anchors could produce up to a five-fold increase in Q for the two lower frequencies. It was found that Q would reach a maximum when $L_a = \lambda/2$, where λ is the wavelength of the primary mode at resonance. When $L_a = \lambda$ the quality factor reached a minimum. This study found no relationship between the width, W_a, and Q and L_a had a negligible effect on the 1.05MHz devices. This paper did not provide any analysis on the cause of this variation in Q but this effect is similar to what is found in Chapter 3 and analysis will be provided then. In addition, this paper makes the assumption that all energy that is transmitted into the anchors is lost to the substrate. This thesis will show that is not the case.

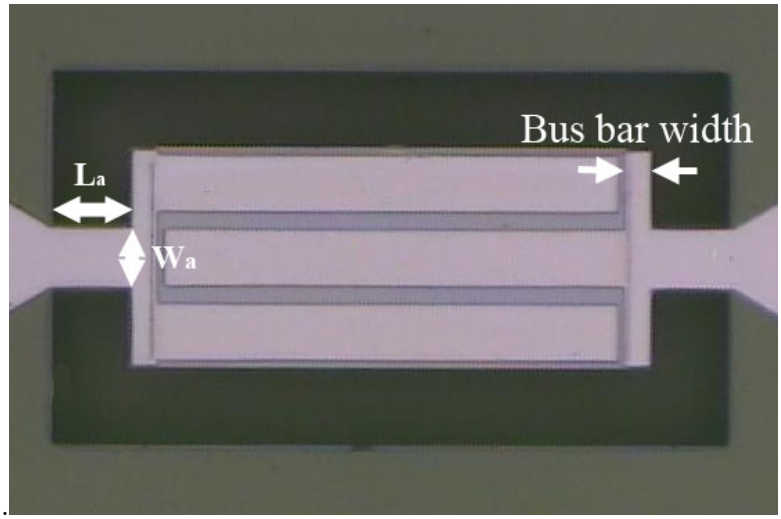

Figure 2.6: The length, L_a, of the anchors of CMRs below 220MHz has a significant impact on performance. It was shown that Q could have a five-fold variation due to anchor length. No correlation between the width, W_a, of the anchors and Q was found.

Much effort has been made to model anchor loss, [24, 25, 26]. These techniques often employ perfectly matched layers (PMLs) [27, 28, 29]. In finite element analysis, a PML is a finite domain attached to the outer boundary of the finite element model to simulate an infinite domain. This is done because the actual MEMS resonator is

several orders of magnitude smaller than the substrate that it is mounted to. It has been assumed that the energy that propagates through the anchors and into the substrate would travel outward with no reflections. This would result in a complete loss of any energy that escapes through the anchors. The PML simulates this effect by matching its mechanical impedance to the device impedance at the boundary. This eliminates any reflection at the interface between the PML and the device. The acoustic wave energy is then exponentially damped out within the PML to eliminate reflections at its outer edges. The simulation can then act like a resonator attached to an infinite substrate. As we will see in chapter 3, this does not perfectly define a real MEMS resonator due to the fact that there is some reflection at the interface between the device layer and the substrate and it is therefore possible to have a portion of the escaping energy return to the resonator.

In addition, [30] studied the anchor losses associated with 65MHz AlN CMRs and offered two approaches for predicting energy losses. The first method is analytical in nature and models the resonator with a one-dimensional wave equation. They assume that the anchors are "quasi-static" meaning that both end conditions are not fixed but the outer edge is more heavily constrained by the substrate. For a given anchor width, w_a, and body length, L, they estimate Q_{anc}, the quality factor associated with anchor loss only to be

$$Q_{anc} = \frac{2\pi(1-\nu^2)^2 L}{\nu^2(W_a + \frac{\lambda}{2\pi} sin\left(\frac{2\pi W_a}{\lambda}\right))} \tag{2.7}$$

where ν is the Poisson ratio of aluminum nitride and λ is the acoustic wavelength of the aluminum nitride layer at resonance. The accuracy of this method at predicting Q is mixed. Of the devices tested, 60% had a predicted Q that fell within two standard deviations of the electrically measured Q. The publication is frank in explaining that this method can serve as a qualitative method for estimating quality factor to help designers

choose device dimensions. The second method for predicting quality factor is numerical in nature and serves to replace the finite element modeling technique of using PMLs in modeling a semi-infinite substrate. It employed a fixed constraint at the edge of the released region and gave results that were considerably more accurate than the first method.

2.5 Interfacial Loss

There are two competing theories on the mechanisms behind interfacial losses. According to [31], this loss mechanism is the result of a stress jump that occurs at the interface of two materials with differing Young's moduli as they undergo strain. For the resonators used in this thesis, this occurs at the interface between the aluminum nitride device layer and the upper and lower metal layers. Aluminum nitride and Aluminum for instance, have significantly different Young's moduli, 308GPa and 69GPa respectively. During operation, as the resonator undergoes elastic deformation, the amount of strain is constant across the interface and therefore there is a jump in the stress value. This stress jump will cause an interfacial slip to occur without breaking the bonds that join the material layers together. This interfacial slip produces unrecoverable thermal energy resulting in energy loss.

The competing theory for interfacial losses follows from the idea of an effective strain jump across the interface as described in [32]. Specifically, there is a jump in acoustic velocity at the interface due to the mismatch in Young's modulus and density between the two materials. This mismatch results in an in-plane strain at the interface which causes energy dissipation due to changes in the crystalline structure. This latter method was validated experimentally using 1GHz aluminum nitride CMRs similar to those used in this thesis.

2.6 Viscous/Air Damping

There are three different mechanisms by which energy is dissipated into the fluid environment surrounding the resonator: acoustic, squeeze-film and viscous damping [33]. When large plate structures are moving normal to their face, acoustic damping dominates. The loss is proportional to the gas pressure. Because the primary mode is in-plane for CMRs, the out-of plane motion is very small and this form of loss is negligible.

Squeeze film damping occurs when two plates move toward each other and, as the name implies, the fluid between the two plates is squeezed out of the way which results in energy loss of the device. This occurs in flexural structures where large in-plane motion occurs or within an inter-digitated comb drive array. Again, because of the nature of the CMR motion this loss mechanism is also negligible. There is a small possibility for this to occur between the ends of the resonator and the substrate but, because the device is less than $2\mu m$ thick, the gap is at least $6\mu m$ wide, and the in-plane motion is less than $1nm$, the result would be orders of magnitude less than other dominant loss mechanisms.

Viscous damping is the result of the solid surface of the reosnator sliding through the viscous atmosphere. This would be the most dominant form of environment/fluid loss in CMRs due to the large plate moving in-plane in atmosphere. Considering this, viscous damping is still not a major source of energy loss due to the fact that there is very little displacement especially at higher frequencies. Experiments have shown [9, 34] that for lateral field excited resonators, the impact on quality factor due to viscous damping is less than 10% at lower frequencies and drops to almost 0% at 1GHz. In fact, [34, 35] show that viscous damping is inversely proportional to the square root of the resonant frequency of the device.

2.7 Thermoelastic Dissipation.

Thermoelastic dissipation (TED) is a process by which energy is lost due thermal gradients brought on by a strain gradient [9, 36, 37]. Elastic strain produces heat. If a strain gradient exists then there will be a thermal gradient and heat flow will result. This heat flux is not recoverable and is therefore an energy loss mechanism. It has been shown in [36, 38, 39] that CMRs suffer from very little thermoelastic damping due to the fact that there is very little displacement and very little resulting strain gradients. At 1GHz, Q would be limited to 32000 which is an order of magnitude higher than experimental measurements.

Chapter 3

Minimizing Anchor Loss

3.1 Background

In an effort to maximize the device Q extensive research has gone into the geometry of contour-mode resonators (CMRs). In [19], it was shown through experimental and simulation studies that the dominant source of energy loss in contour-mode resonators below 400MHz was due to anchor losses. Three device frequencies were tested: 220MHz, 370MHz, and 1.05GHz. For each frequency, multiple anchor dimensions were tested. For the two lower frequencies, the quality factor improved when the width of the anchors approached $\frac{1}{2}\lambda$, where λ is the acoustic wavelength of aluminum nitride. The quality factor decreased when the width of the anchor approached λ. This trend was not evident in the 1.05GHz devices. For the high frequency devices, there was also no trend with regards to the length of the anchors and at higher frequencies, interfacial dissipation becomes more dominant as shown in [32].

The dimensions of the bus bars has also been studied as a source of Q degradation in CMRs. Because the bus bars (see figure 3.5) are outside of the active region, they do not aid in the transduction of mechanical and electrical energy but they can serve to enhance

the performance of the active region. In [18] the widths of the bus bars are varied in a group of 207MHz CMRs. When all other device dimensions were held constant, a 40% increase in Q was found when the bus bar width was optimized. The paper provides no analytical insight into why the bus bar width effects Q except to explain that, by varying this dimension, the "equivalent acoustic boundary condition" (the edge of the active region) is being transformed. Section 3.5 of this thesis provides analysis on a phenomenon that is very similar to the results of [18] and can support this theory.

In [40] the shape of the electrodes are tailored to minimize spurious modes. Called apodization, the lengths of the electrodes are contoured to minimize the excitation of other, unwanted modes in the body of the CMR. While this techniques does not increase Q, the elimination of spurious modes may help in reducing phase noise.

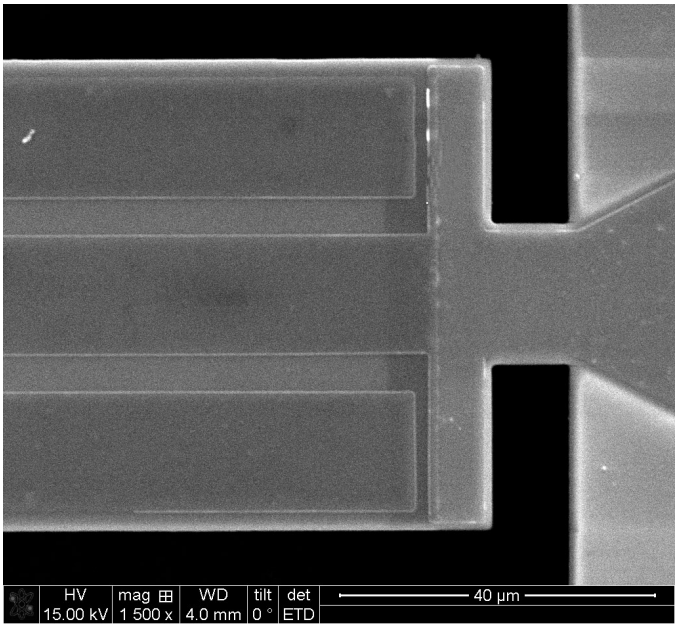

Figure 3.1: An SEM image of the anchor region of a 220MHz AlN CMR. Typical studies assume that the outer edge of the anchor (right side in this image) are fixed to the substrate and do not undergo displacement.

Yet to be considered is how the quality factor is affected by the propagation of acoustic waves into the substrate region beyond the anchor attachment points. When modeling

resonators, it is often assumed that the outer end of the anchor is fixed with respect to the substrate (figure 3.1). This simplifies analysis but is not completely accurate due to the fact that an isotropic etch process is often used to release the device from the substrate [41]. This etch also releases the device layers outside of the anchor region from the substrate (figure 3.2) making the resonator more compliant than a traditional model would indicate. Through laser Doppler vibrometer (LDV) measurements it was determined that the outer end of the anchor in a 220MHz resonator can move as much as 60pm in the out-of-plane direction which is approximately 20% of the maximum magnitude of motion seen in the body of the resonator. This motion results in strain energy that can be lost to thermoelastic dissipation resulting in a degradation of Q.

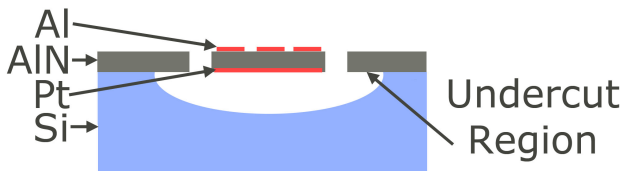

Figure 3.2: The isotropic etch that is used to release the device from the substrate also undercuts the region outside of the device anchors. This results in excessive motion that can effect the quality factor by as much as 31%.

To determine the effects of this substrate motion, the out-of-plane displacement of multiple 220MHz aluminum nitride (AlN) CMRs were measured using an LDV along a path shown in figure 3.3. Electrical measurements were also taken to monitor Q and the fundamental contour-mode resonant frequency, f_0. The device then underwent a XeF_2 etch to release additional device layer area. The measurements were then taken again. This sequence was repeated nine times. We show that there is a variation in Q of up to 31% due to the motion of the released region and that this variation occurs as a function of L, the distance from the active region of the device to the edge of the released region of the device layer (figure 3.3). This effect is explained through the use of transmission line theory and also by the appearance of standing waves in the released region.

To further validate this theory, a design change was made to the device layers in the released region, converting the outer boundary condition from a fixed to a free condition. In doing so, the quality factor of the device switched from a minimum to a maximum.

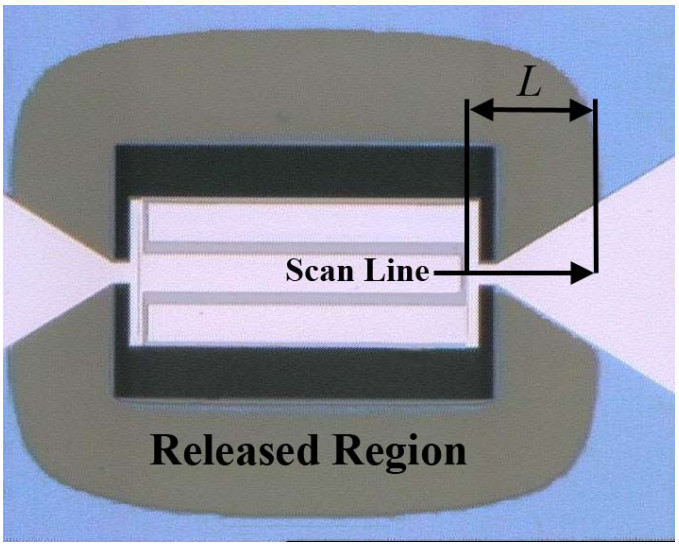

Figure 3.3: A schematic of the measurement path of a heterodyne laser Doppler vibrometer. Also shown is the released region of the device layer that is outside of the anchors (dark area). This is due to the isotropic XeF_2 etch that is used to release the body of the device from the substrate.

3.2 Alumnium Nitride CMRs

The devices used for this study are AlN-based CMRs [18]. These are piezoelectrically actuated devices composed of a $1\mu m$ AlN layer sandwiched between upper and lower $100nm$ metal layers (figure 3.4). The upper layer is patterned to provide interdigitated drive and sense electrodes that govern the contour-mode resonant frequency. The bottom electrode layer covers the entire device in order to contain the electric field. The body of the resonator measures $140\mu m$ long and $57\mu m$ wide. The resonant frequency, f_0 is set

by the electrode spacing and is governed by [9]

$$f_0 = \frac{1}{2W}\sqrt{\frac{E_{eq}}{\rho_{eq}}} \tag{3.1}$$

where W is the electrode spacing (figure 3.4) and E_{eq} and ρ_{eq} are the Young's modulus and density respectively of all three layers combined. By applying an sinusoidal voltage to the electrodes at the device's resonant frequency, in-plane Lamb waves are induced as a result of the strain produced by the d_{31} Piezoelectric coefficient of the aluminum nitride.

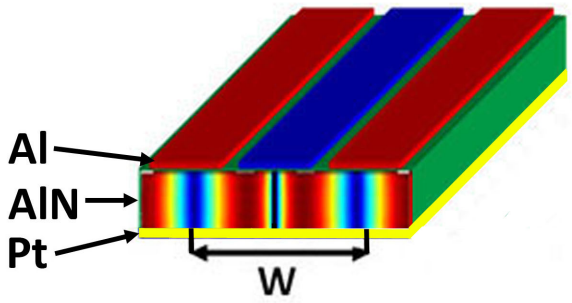

Figure 3.4: The devices are composed of a $1\mu m$ aluminum nitride layer sandwiched between a 100nm upper and lower layer of aluminum and platinum respectively. The operating frequency of the resonators is set by the electrode spacing, W. When driven at this frequency, in-plane Lamb waves are created as a result of the d_{31} Piezoelectric coefficient of the AlN.

The devices are fabricated by first applying a 10nm layer of titanium to provide adhesion between the silicon handle wafer and the 100nm aluminum layer that is deposited next to serve as the bottom electrode. A $1\mu m$ device layer is then sputtered and subsequently followed by the top 100nm, patterned electrode layer of platinum that is evaporated on. A CL_2-based dry etch is used to pattern the AlN layer. The final step is an isotropic XeF_2 etch to release the device from the substrate. It is this final etch step that also releases the region outside of the anchors. During fabrication, often the priority is to insure a complete release of the device without concern for the effect of this

released substrate region. This study shows that it can have a profound effect on device performance.

Acoustic energy is produced in the active region of the resonator which includes the area between the tips of the electrodes (figure 3.5). Energy contained within the active region can be used for transduction whereas energy that escapes into the adjacent inactive regions, which includes the bus bars, anchors and released regions, results in a degradation of the quality factor unless it can be reflected and returned to the active region.

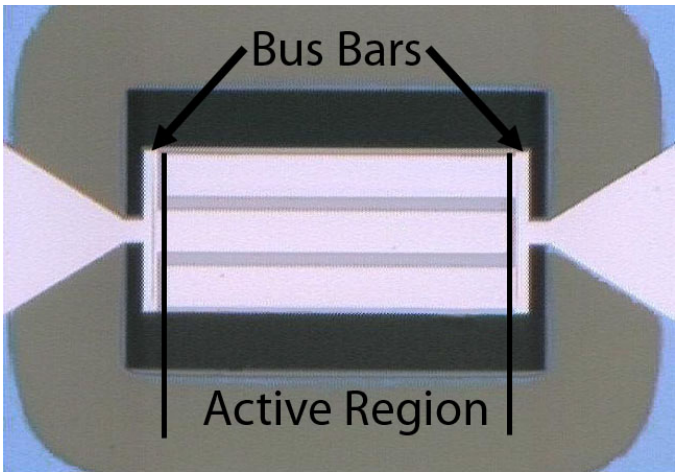

Figure 3.5: The acoustic energy used for transduction is produced within the active region of the resonator. Energy is dissipated into the inactive regions where it could potentially be reflected and returned to the active region or it could be dissipated into the substrate where it contributes to a loss in quality factor.

3.3 Experimental Measurements

In a contour-mode resonator the primary motion is in-plane which cannot be directly measured using LDV. There is, however, measurable out-of-plane motion due both to the Poisson effect and the Piezoelectric effect. To this end, using COMSOL, a finite element model was built which included perfectly matched layers (PMLs) [42, 28] to simulate the

devices. The FEA model was validated by matching its out-of-plane motion with that of the LDV measurements. This is discussed in section 3.4. The energy flux through the resonator anchors produced by FEA could then be compared to the released substrate length, L.

Admittance data was collected using a Rhode&Schwarz ZVL vector network analyzer (VNA). The device was probed using an Infinity probe from Cascade Microtech (model I40-A-GSG-150)and the VNA was calibrated using a Cascade Microtech impedance standard (part# 101-190). From the electrical data f_0 and Q were extracted. Appendix D describes how these values are found from the admittance data.

The out-of-plane displacement measurements were taken using a Polytec UHF120 LDV. A 50X objective was used to produce a spot size of approximately 2μm. The device was driven using a Rhode&Schwarz SMBV100A function generator (FGN). The device was probed in the same setup as the electrical measurements. It was scanned with the LDV along the path shown in figure 3.3 with a spatial resolution of 720nm $\pm$80nm. This allowed us to look at the displacements of the body of the resonator, both anchors and the released area outside of the anchors. The device was driven at -6dBm and at its resonant frequency determined by the electrical measurements. This power level was chosen to prevent the resonator from operating in a nonlinear regime while still inducing enough out-of-plane motion to be detectable with the LDV. Displacement data was collected with an out-of-plane resolution of 1.2pm and with a noise floor of 4pm. Displacement magnitude values were extracted from a fast Fourier transform of the original LDV time trace with a resolution bandwidth of 19.5kHz.

Table 6.1 shows the details for the three resonators that were tested for this study. They operate in the 220MHz range with similar electrode configurations but each have different anchor dimensions and their initial quality factors vary from 1176 to 2588.

Table 3.1: The resonant frequency, quality factor, anchor dimensions, and bus bar width of the devices tested (see figure 2.6).

Device #	f_0 [MHz]	Initial Q	Anchor Length $[\mu m]$	Anchor Width $[\mu m]$	Bus bar Width $[\mu m]$
1	218.39	1866	7.5	8	6.59
2	220.58	2588	21	15	7.33
3	220.75	1176	11	15	6.96

3.4 Finite Element Modeling

In order to verify that the motion measured in the released region is proportional to the energy loss through the anchors, a COMSOL Multiphysics model of the resonator body, anchors, and surrounding substrate was made. The geometry of the model was taken from device #1, and PMLs were used to model the semi-infinite substrate [42, 28, 43]. The PMLs were used at the edges of the silicon and aluminum nitride layers and on the upper electrode layer near the region of interest (shown in black in Figure 3.6). The PMLs were placed $300\mu m$ from the outer edge of the anchor in the direction of the scan path. This distance is far enough from the edge of the released substrate region so that any reflections at this interface could be taken into account in the simulations. The simulated magnitude and wavelength of the out-of-plane displacement were compared to that of the LDV measurements in the inactive region of one side of the resonator to validate the model. The model was then simulated for each release distance, L, from the experimental procedure and the energy flux through the outer cross-section of the anchor (Figure 3.6) for each release distance was calculated. The results of the simulations and experiments are given below.

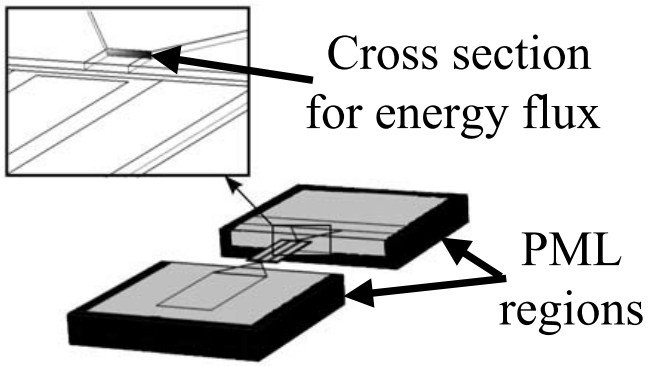

Figure 3.6: COMSOL FEA was used to compute the energy flux through this cross section in the anchors over one cycle. Perfectly matched layers (shown in black) were used to simulate a semi-infinite substrate. The simulation was validated by matching the out-of-plane motion to the LDV experiments.

3.5 Analysis and Results

Figure 3.7 shows the LDV measurements and COMSOL simulation of the displacement of the substrate region for one side of the device before any additional etching. This quality of fit for the displacement and wavelength of the simulation to the LDV data validated the COMSOL model.

To provide a figure of merit that is proportional to strain energy, the measured displacement is squared and then the area under this curve is integrated to provide a single value that is proportional to the energy being transmitted into the inactive region,

$$FoM = \int_0^L D(x)^2 dx \tag{3.2}$$

where $D(x)$ is the magnitude of the displacement at a point x along the LDV scan path. This is done for each etch step and is plotted in figure 3.8 for all three devices as a function of L normalized to the wavelength, $\lambda = 48.08\mu m$. This value for λ was found by performing a spatial FFT on the displacement curve of device #1. This method is explained in detail in Chapter 5. This allowed us to determine the actual acoustic

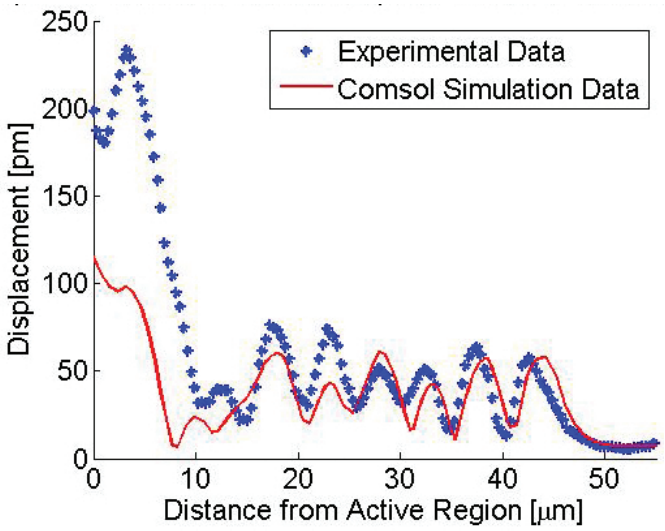

Figure 3.7: The experimental and COMSOL simulated displacement of the released region of device #1. The exceptional match of the simulated and LDV data validated the COMSOL model, allowing the energy flux through the anchors to be evaluated.

wavelength of the sputtered aluminum nitride in the tested devices. Because of variations in the sputtering process, the density and elastic modulus can change from batch to batch which will alter the acoustic velocity and the wavelength.

A portion of the acoustic wave energy generated within the active region of the resonator propagates outward into the bus bar and anchor regions. The portion that passes through the anchor then travels into the released portion of the substrate. These elastic waves reflect off of the outer edge of the released region and a portion can return to the active region of the resonator. This effect can be analyzed using electrical transmission line theory [44, 45].

Figure 3.9 shows the transmission line model as it is applied to the resonator. The active region is represented as an AC voltage source with some characteristic impedance, Z_0. The inactive region can be modeled as a transmission line with its own impedance. The outer edge of the released region is fixed to the substrate and therefore the bulk of the acoustic energy is reflected. This condition, in electrical terms, can be treated as an

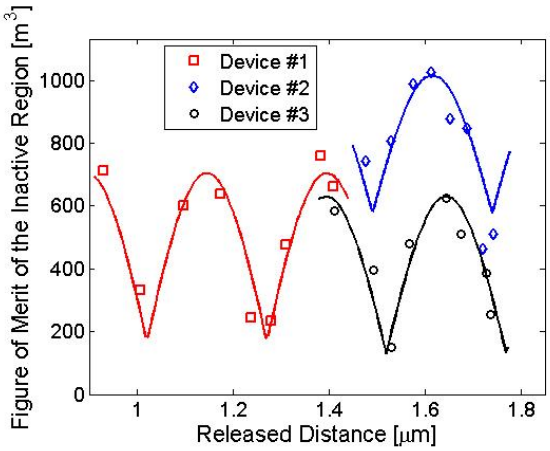

Figure 3.8: The magnitude of the displacement of the released region was squared and the area under the curve was integrated to provide a figure of merit proportional to strain energy. this figure of merit follows an $abs(sin)$ pattern as explained below.

open circuit. Due to this open circuit condition, the impedance of this transmission line as seen by the active region is

$$Z_{out} = \frac{-jZ_0}{\tan(kL)} \tag{3.3}$$

where k is the wave number associated with the resonant frequency and L is the length of the inactive region. Appendix E goes into detail about transmission line theory and of the derivation of this equation. Since the device has the same composition throughout the active and inactive regions, the impedance, Z_0 of each section is identical for the purposes of this study. It can therefore be shown that the traditional power equation, $P_{esc} = I \cdot V^*$, showing the loss of energy to the inactive region of the device becomes

$$P_{esc} = \text{abs}\left(V^2 \frac{\sin(2kL)}{4Z_0}\right) \tag{3.4}$$

Equation 3.4 shows that the minimum energy is transmitted from the active to the inactive regions when $L = n\lambda/4$ where $n = 1, 2, 3...$ is the number of wavelengths contained

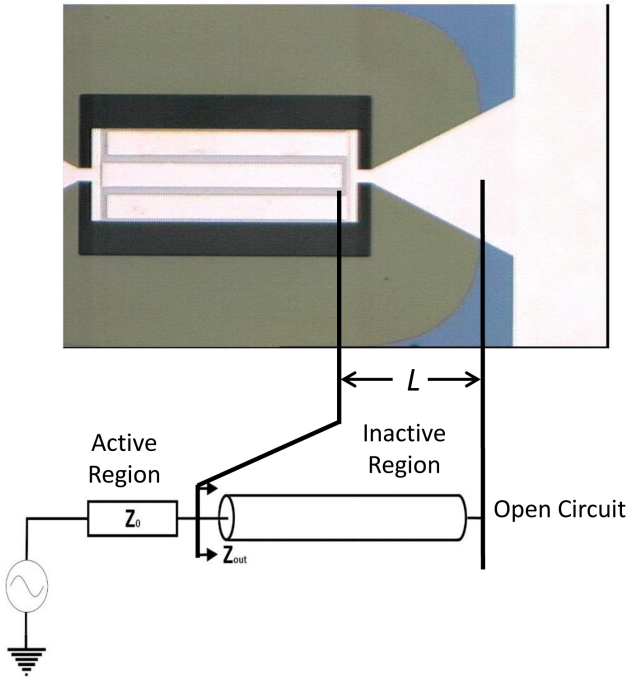

Figure 3.9: Using transmission line theory to describe the energy flux through the anchors, the active region is modeled as a voltage source with a characteristic impedance and the inactive region is modeled as a transmission line. Because the outer edge of the released region is fixed to the substrate, it can be treated as an open circuit. Under this condition, all of the acoustic energy is reflected.

within the inactive region. Under this condition, the current and voltage are in quadrature, meaning that they are $\frac{\pi}{2}$ radians out of phase with each other. When $L = 2n\lambda/4$ the inactive region acts as a $\frac{1}{2}\lambda$ transformer and places a virtual fixed boundary at the edge of the active region (figure 3.10). The electrical equivalent is that the current flow, $I = 0$, and the power transmitted to the end of the transmission line is zero. When $L = (2n-1)\lambda/4$ the inactive region acts as a $\frac{1}{4}\lambda$ transformer by placing a stress-free boundary at the edge of the active region. In this case, the electrical equivalent is that the voltage, $V = 0$, and the power transmitted to the end of the transmission line is zero. Either of these conditions confines the maximum amount of acoustic energy into the active region and minimizes the energy lost to the anchor/substrate region. This is evidenced by the minima in figure 3.8.

The figure of merit for the inactive region of the simulation also follows the same $abs(sin)$ trend as the experimental measurements (figure 3.11). From the simulation, the energy flux through the anchors was measured and plotted in figure 3.12. It follows an identical trend to the figure of merit of the displacement of the inactive region, validating the theory that anchor motion is proportional to energy loss through the anchors.

The figure of merit was found for the active region and the ratio of active to inactive regions is plotted in figure 3.13. As expected, there is an inverse relationship between figure 3.8 and figure 3.13. When there is a minimum in the motion of the inactive region, there is a peak in the active/inactive ratio. Because the voltage produced by a piezoelectric device is proportional to strain this ratio is proportional to the quality factor. A similar equation from [44] was modified to account for the released area:

$$\widetilde{Q} = \frac{Q_{ideal}}{1 + 2\alpha\left(\frac{2abs(sin(2kL))}{4Z_0}\right)} \tag{3.5}$$

where Q_{ideal} is the ideal Q with no anchor loss, and α is proportional to the amount

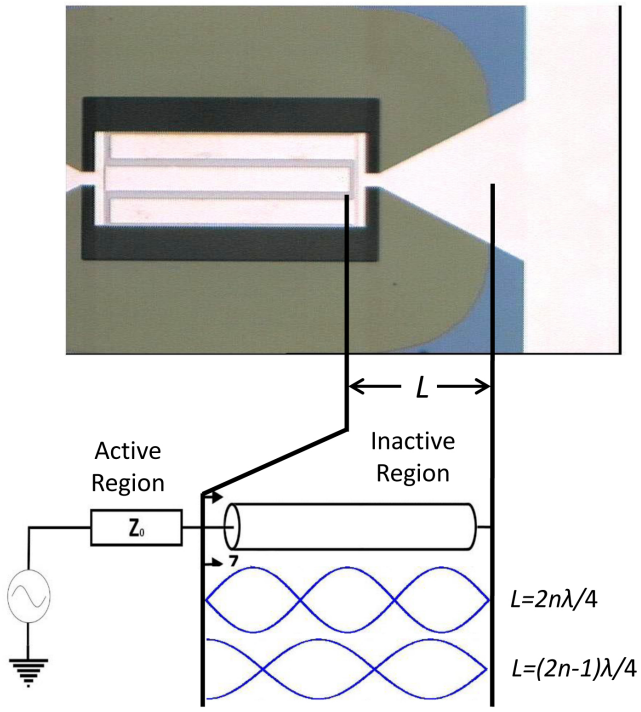

Figure 3.10: When the length, L of the inactive region is equal to an integer multiple of $\lambda/4$ it acts as a either a $1/4\lambda$ or $1/2\lambda$ transformer. This constrains the maximum amount of energy within the active region of the resonator and therefore maximizes Q.

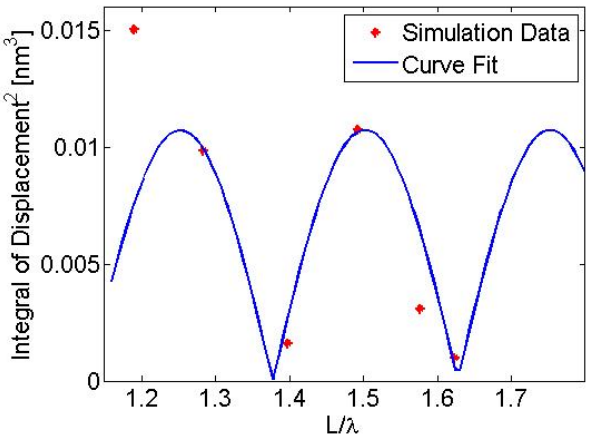

Figure 3.11: The figure of merit for the displacement of the inactive regions of the COMSOL Simulations at each etch step and the analytical fit as a function of the wavelength, λ, from the active region. Maximum displacement occurs every $12.02\mu m$, which corresponds to $n\lambda/4$. The simulation data follows the same trend as the LDV measurements.

of energy lost to the anchor from the active region of the resonator. An identical $\lambda/4$ variation can be seen for Q with peaks at $n\lambda/4$ (figure 3.14). The quality factor varies by as much as 31 % for device #1. Each of the devices tested had different baseline Q values because each had different anchor lengths and bus bar widths. Because of these dimensions, they each had different levels of energy that is dissipated to the released region.

3.5.1 Released Region Modification

To further validate the theory that some of the escaping energy through the anchors is recoverable, a slot was cut through all three layers of device #3 in the released region (figure 3.15). It was placed at a distance of $L \approx 1.625\lambda$ from the edge of the active region. Before this modification, when $L = 1.625\lambda$, the quality factor was 2475, which represents a minimum value. Placing a slot at this point converts the boundary condition from a

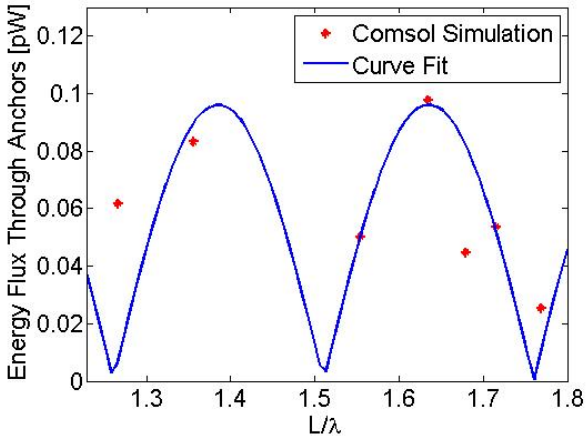

Figure 3.12: The simulated energy flux through the anchors of the resonator over a complete cycle. A minima occurs every $n\lambda/4$. This occurs as a result of the inactive region acting as a $1/4\lambda$ or $1/2\lambda$ transformer and placing a stress free or a virtual fixed-boundary condition at the edge of the active region. This serves to contain the acoustic energy within the active region of the resonator, improving Q.

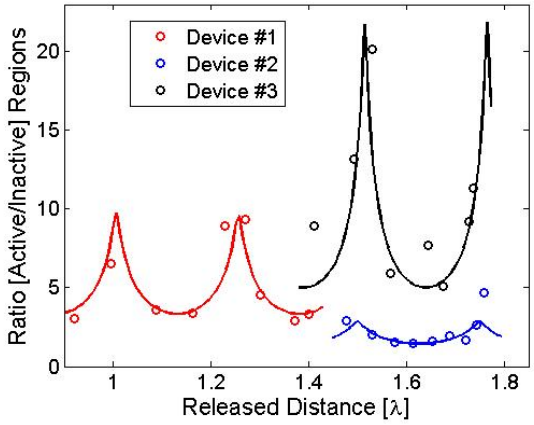

Figure 3.13: A figure of merit identical to that used for the inactive region was used for the active region and the ratio of these two is shown as a function of λ. The resulting value is proportional to Q and follows the same trend (solid lines). When there is a minimum in anchor displacement, there is a peak in this ratio.

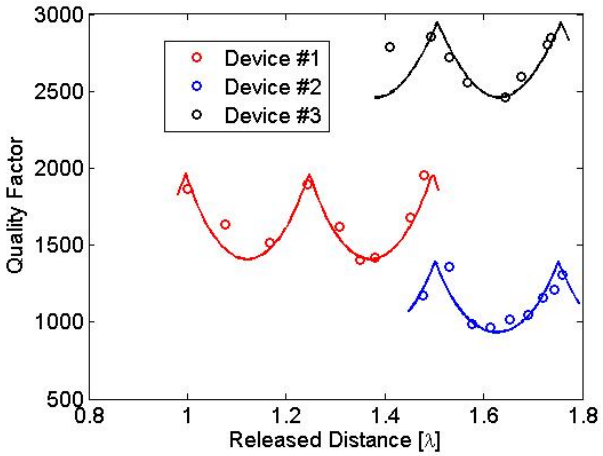

Figure 3.14: The quality factor at each etch step. Q varies by as much as 31% as the etch distance is varied. The maxima at $n\lambda/4$ correspond to points of minimum energy loss through the anchors. The solid lines are curve fitting of the $abs(sin)$ function.

fixed to a stress-free edge. The outer edge of the released region is therefore converted from a node to an anti-node. In transmission line theory, this would result in the end condition becoming an ideal terminated end rather than an open circuit. The quality factor at $(L = n\lambda/4 + \lambda/8)$ reached a maximum value of 3048 as opposed to a minimum value of approximately 2475. In fact, this Q is highest value obtained for this device. A second slot was cut at $L \approx 1.375\lambda$ with similar results. A Q of 2940 was obtained. Without the slot, the Q was 2575 at this value for L. Similar to [45], with these slots through the device layer, the release distance will no longer effect the performance of the device. The boundary for wave reflection is now set by the slot and not the edge of the released region.

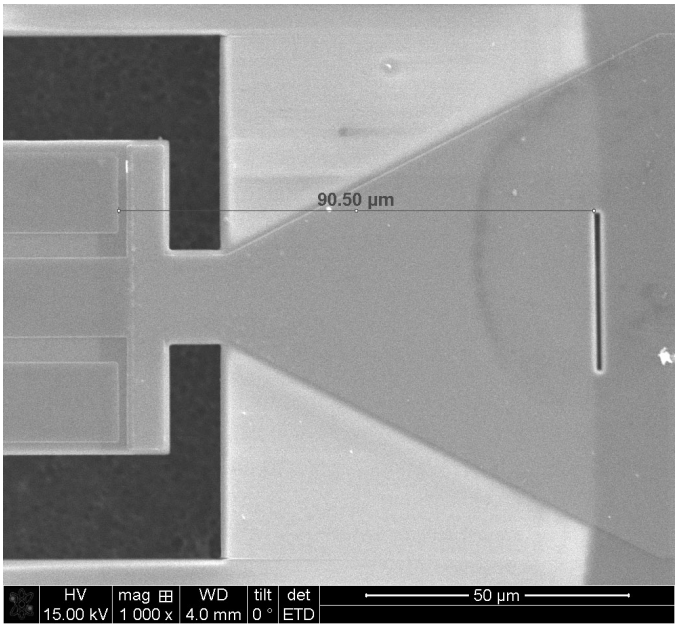

Figure 3.15: Using a FIB, a slot was cut through the device layers of the released region ($1\mu m$ x25 μm). This converted the end condition from a node to an anti-node. The result is that, at $(n\lambda/4 + \lambda/8)$, Q reaches a maxima.

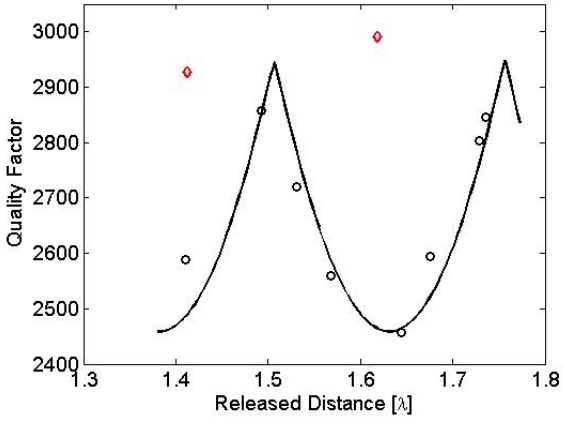

Figure 3.16: Due to the fact that the end condition of the released region has been converted from a fixed to a stress-free condition, the previous minimum Q points at 1.375λ and 1.625λ become maximum Q points. In fact, the highest Q for this device (#3) was obtained with the stress-free end condition.

3.6 Conclusion

As we have seen the isotropic XeF_2 etch step releases not only the device, but the device layers outside of the anchor region. The quality factor of the device can be very sensitive to this etch distance. In some cases a variation of length, L, by $1\mu m$ can result in a degradation in Q by 11%. During a commercial fabrication process this etch step could be difficult to control with the precision necessary to minimize energy losses. As a result, an effective alternative would be to incorporate slots into the released region rather than trying to control the etch rate of the XeF_2 . Doing so could produce a gain of up to 31% versus allowing the release etch to go uncontrolled. This could also be necessary if multiple resonators of differing frequencies are placed on the same die.

3.7 Future Work

Additional studies could be performed on resonators at both higher and lower frequencies. As operational frequencies increase, the wavelengths decrease. As a result, very small changes in the released distances can have potentially very large effects on Q. It is believed that at higher frequencies, anchors losses have a much smaller effect on Q and carrying out a study similar to this one could help confirm that. Conversely, a similar study on low frequency devices could highlight the need for careful design of the anchors and anchor regions. It would also be interesting to optimize the design of both the bus bar and the anchor dimensions and then perform this study again to see what effect, if any, the released region has on a device with already minimized anchor losses. It is possible that, at some point, the amount of energy that escapes through the anchors is so low that it is not possible to recover any of it. It may also be possible that these slots should become a feature of all future designs to capture any additional energy that

escapes through an otherwise optimized design.

Another line of study would be to experiment with methods to fabricate the wave reflectors and properly incorporate them into the initial designs of the devices. The placement could be much more carefully controlled during initial fabrication as opposed to using a FIB to cut them. Alternatively, a new fabrication process could be developed to eliminate this undercutting process completely. If the devices could be fabricated so that the outer edge of the anchor was actually fixed to the substrate, modeling the devices could prove to be much more accurate than in the past.

Chapter 4

A New Method for Single Point Ring-Down Measurements

4.1 Introduction

A common characterization of resonant structures involves performing a ring-down measurement. This measurement provides information about the device's quality factor as well as non-linear characteristics that may be present. Due to a very low signal to noise ratio and trigger inaccuracy, the process of measuring ring-downs at ultra high frequencies is not possible with the traditional ring-down methods. This chapter describes a new method for performing ring-downs on ultra high frequency resonant structures with very low displacements using laser Doppler Vibrometry (LDV). The measurements performed on the devices in this study produced quality factors that were all within 6% of the electrically determined values for Q. The devices tested were 220MHz alumnium nitride (AlN) contour-mode resonators (CMRs) but this technique could be extended to both lower and higher frequencies (potentially up to the 1.2GHz limit of the UHF-120 vibrometer) and to other bulk mode and flexural mode structures.

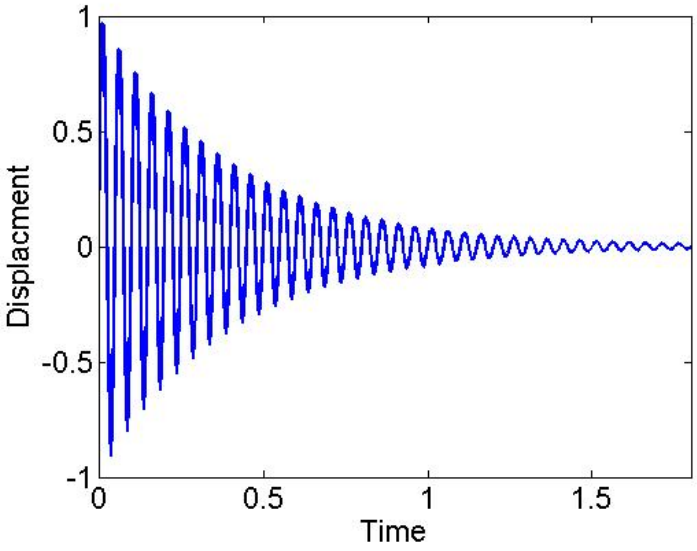

Figure 4.1: An example of the exponential decay profile of a traditional, linear resonant device. The rate of decay is defined by a ring-down time constant, τ.

4.2 Theory

Traditional ring-down measurements are performed by applying a step function to the DUT and then measuring its response to this input [46, 47]. The harmonic motion of a linear resonant device will decay exponentially over time, t, to zero following the equation

$$x(t) = A_0 \exp(\frac{-t}{\tau}) sin(\omega_0 t) \tag{4.1}$$

where ω_0 is the resonant frequency of the device, A_0 is the initial magnitude, and τ is the ring-down time constant. Figure 4.1 shows an example of this decay. The rate at which this motion decays is defined τ. A larger value for τ will result in a longer ring-down time. The quality factor of a resonantor is directly related to τ

$$Q = \pi f_0 \tau \tag{4.2}$$

where f_0 is the resonant frequency.

To capture the complete ring-down event, the LDV measurement must be started before the drive signal has been switched off and it must continue until the motion of the resonator has decayed to zero. To ensure that the complete ring-down is captured by the vibrometer, the timing between the cut off of the applied signal and the start of the measurement must be carefully timed.

During steady-state operation, the surface of the CMRs tested in this study had a maximum out-of-plane displacement of between 100 and 400pm. At this amplitude, the vibrometer output signal is dominated by noise. This noise comes from various sources including thermal noise in the resonator and inherent measurement noise in the LDV. Figure 4.2 shows a comparison between an ideal, simulated ring-down time trace and an actual ring-down measurement taken from a 220MHz CMR by the Polytec UHF-120 LDV. Figure 4.3 shows the device used for this measurement. A detailed description of the device is given in chapter 2.2. The measurement was taken at the center of the device. It is evident that the ring-down signal is completely buried in noise.

In order to reduce this noise, it is necessary to take multiple measurements and average them together. The Polytec VibSoft software used to control the UHF-120 vibrometer has the ability to do this automatically for up to 10,000 cycles. Unfortunately this system has an inherent trigger error of ±4ns. This error is negligible at lower frequencies but at 220MHz the period of a single wavelength is 4.55ns and as a result, repeated averaging will eliminate the desired ring-down signal along with the noise. Figure 4.4 shows a simulation of this effect. The original, 220MHz simulated signal (blue trace) was averaged only ten times with a timing error of ±4ns which resulted in a ten fold decreasing in signal amplitude (red trace). To suppress this inherent random noise Polytec recommends

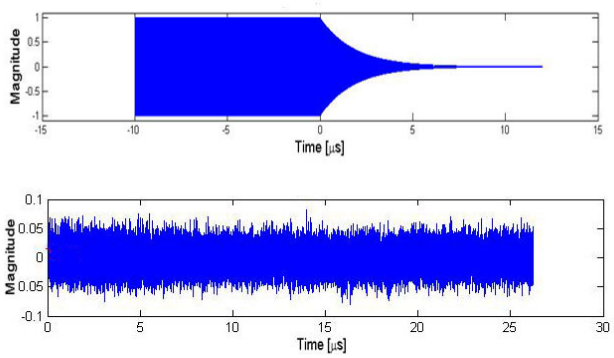

Figure 4.2: A comparison between an ideal ring-down profile and the actual LDV measurement of the ring-down of the 220MHz resonator. The signal is dominated by noise due to the small displacement. No averaging was applied to this time signal.

averaging up to 10,000 times. At this frequency and amplitude, it is not possible to make use of time domain data to measure a ring-down.

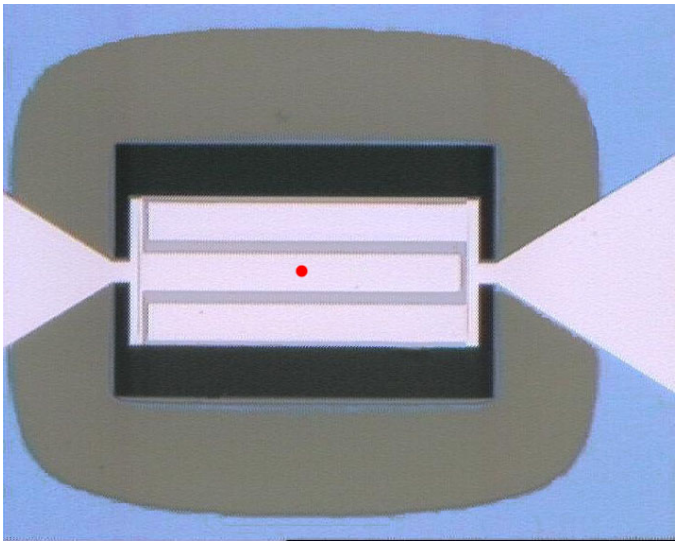

Figure 4.3: An example of the 220MHz AlN CMR used for single point measurements. These measurements were taken at the center of the device (red dot). Initial displacements ranged from 125pm to 225pm.

The solution is to make these measurements in the frequency domain as opposed to the time domain. In frequency domain measurements, the LDV takes a discrete time sample and performs a fast Fourier transform (FFT) to extract the magnitude and phase

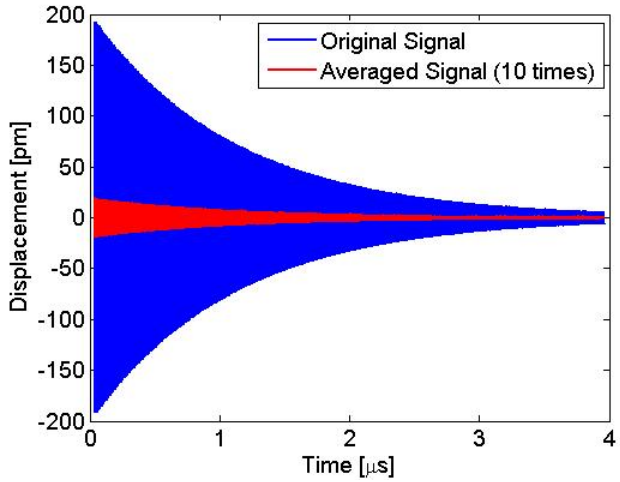

Figure 4.4: A simulation of the reduction in signal amplitude due to averaging ten times when a trigger error of ±40ns exists. To suppress the noise, Polytec recommends averaging up to 10,000 times.

information of the various frequency components in the time sample. The magnitude and phase data is then averaged over successive measurements in order to suppress the noise. The two methods for averaging that are most commonly used in vibrometry measurements are magnitude and complex averaging. Appendix A.2 gives detail on these two methods and for these measurements, complex averaging is the preferred method because it is much more effective at suppressing noise due to Brownian motion and other incoherent noise. In the frequency domain the trigger error becomes negligible because the ±4ns error is three orders of magnitude smaller than the $3.2\mu s$ sample time used for the FFT measurements.

To measure the decaying amplitude of a ring-down profile, short time samples are taken of only a portion of the transient event. The timing between when the measurement starts and when the drive signal is cut off is progressively delayed so that short samples are taken along multiple time points of the ring-down. Figure 4.5 shows an example of three such delay points. The magnitude of the resonant frequency for each sample is then used to reconstruct the ring-down. For the example shown in figure 4.5, a sample time of

$8\mu s$ was used and the time step between each sample was $10\mu s$. In practice, many more time points should be taken so that each time sample overlaps the previous one. This will insure high enough time resolution of the ring-down profile.

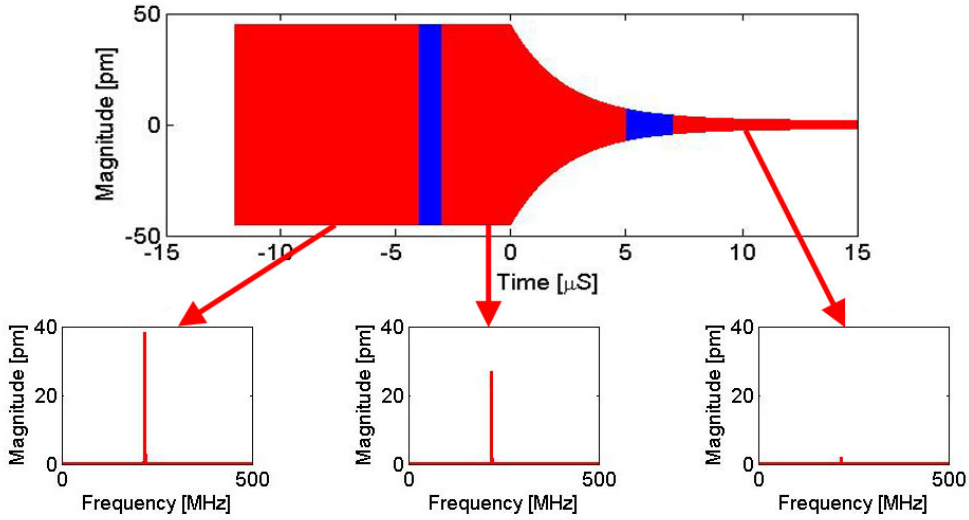

Figure 4.5: An FFT is taken from short time samples at multiple time points throughout the ring-down event. For clarity, this example used $8\mu s$ time samples that were taken every $10/mus$. In practice, many more points at shorter intervals should be used. The magnitude at each time point is then used to reconstruct the ring-down.

4.3 Experimental Setup and Results

Figure 4.6 shows the measurement setup. A function generator produces a square wave at approximately 1kHz to provide timing for the simultaneous triggering of the start of the measurement and termination the sinusoidal drive signal. The device is driven with a Rhode&Schwarz SMBV100A function generator at the device's resonant frequency and at -6dBm. At this power level, nonlinear effects due to heating are not observable but there is still sufficient surface displacement to achieve good LDV displacement data.

The resonant frequency and device electrical quality factor are determined by col-

lecting admittance data using a Rhode&Schwarz ZVL network analyzer. The analyzer was calibrated using a Cascade Microtech calibration standard. The device was probed using an Infinity probe from the same company. The delay between the cut-off of the drive frequency and the start of the measurements was automated using software written by this author. Detail of this software is given in Appendix B. All other measurement parameters such as drive frequency and power were also controlled by this software.

Six devices were used for this study and an example is shown in figure 4.3. The body of the resonators measure 140μm long by 58μm wide. They consist of a 1μm thick aluminum nitride layer sandwiched between an upper and lower 100nm layer of aluminum and platinum respectively. Each device had identical geometry except for the length and width of the support anchors. Table 4.1 gives these dimensions for each device.

Figure 4.7 shows the experimental measurements from a single spatial point at the center of the body of resonator #1 with a sample time of 3.2μs and a time step between each sample of .2μs. The sampling rate was 2GHz. Each time point was averaged 100 times using complex averaging (see Appendix A.2 for detail on averaging).

It is necessary to optimize the sample time. If the sample time is too long, the portion of the sample that represents the ring-down event becomes too small and the amplitude resolution will decrease. The sample time must also be long enough to avoid FFT bin splitting. When the sample time is short the resolution bandwidth (RBW) of the FFT becomes large. This means that the bin spacing becomes larger. If the time sample contains a frequency that is not aligned with the center of an FFT bin, its magnitude data is split between two adjacent bins. Doing this will give erroneous data. In order to avoid this, the drive frequency must be selected to line up with the center of one of the FFT bins. This means that, to get good data, the drive frequency may be slightly off from the devices resonant frequency. Therefore, the sample time must be long enough to ensure that there is a small enough RBW to allow for a drive frequency that is close to

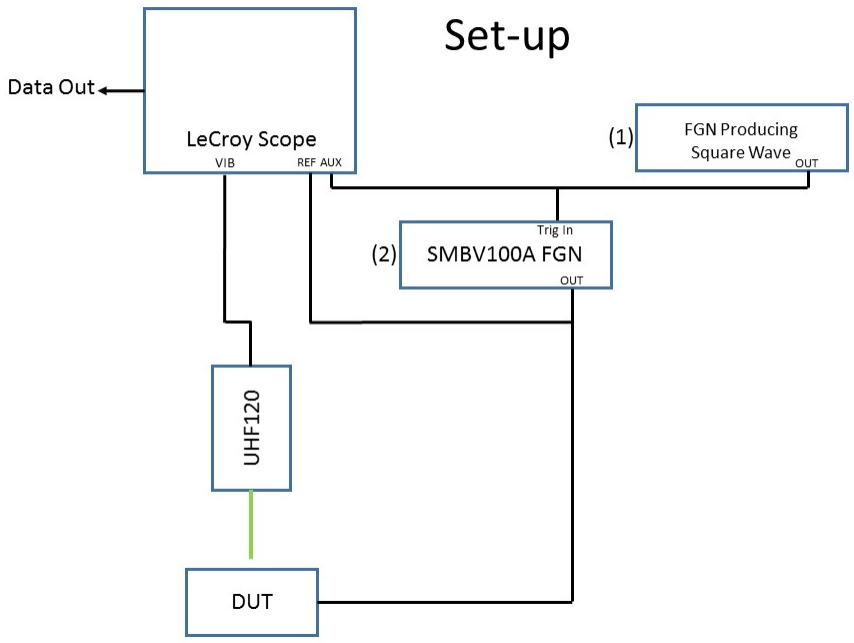

Figure 4.6: The measurement setup for capturing ring down measurements of a 220MHz CMR. The first function generator is used to trigger the start of the measurement and the cut-off of the drive signal supplied by the second function generator. The LeCroy scope is used to capture the data from the vibrometer and transfer it to the PC for post-processing.

the device's resonant frequency.

The experimental data in figure 4.7 does not follow the expected exponential decay of a traditional ring-down. This is due to the fact that each data point is the average magnitude of the resonant frequency over its entire time sample. For example, if the sample window includes steady-state oscillation as well as a portion of the ring-down event (e.g. the center FFT in figure 4.5) the magnitude is a convolution of the steady-state and the ring-down event. The most efficient way to determine the ring-down time constant is to produce a simulated waveform that includes a steady state and ring-down event and perform a simulated measurement with identical parameters to the experimental measurement. The frequency, steady-state magnitude, sampling rate, drive signal cutoff

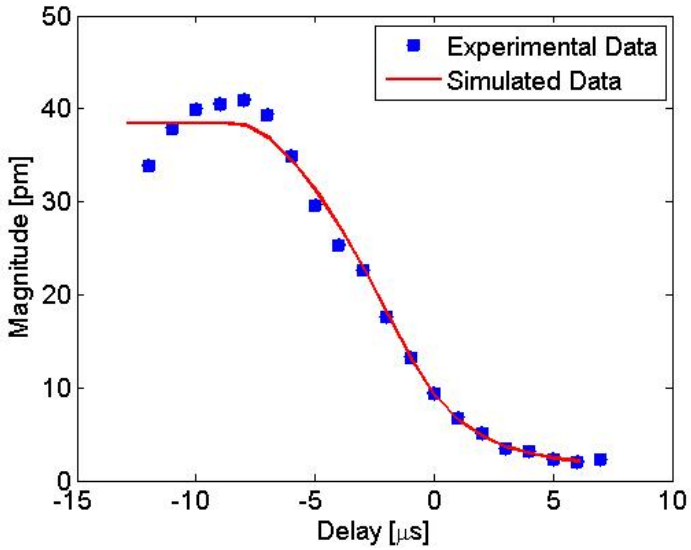

Figure 4.7: An FFT is taken from short time samples at multiple time points throughout the ring-down event. The magnitude at each time point is then used to reconstruct the ring-down.

time and sample time are all know a priori. The time-constant, τ, for the exponential decay can then be varied until there is a good fit between the experimental and simulated data. Figure 4.7 shows the match between the experimental and simulated data from the single spatial point at the center of the device. For this measurement the time constant $\tau = 2.4\mu s$. At the resonant frequency of 220.5MHz this gives a quality factor of 1664 which matches the electrically measured Q of 1610 by 3.25%.

Five other devices were tested for this study. Table 4.1 shows the results of these measurements. All of the LDV ring-down measurements are within 5.25% of the electrical quality factor. Devices with higher electrical Q resulted in more precise measurements which is most likely due to the fact that these devices have higher initial displacements, which results in less noise.

Device #	$f_0[MHz]$	Anchor Length $[\mu m]$	Anchor Width $[\mu m]$	Initial Displacement [pm]	Electrical Q	$\tau[\mu s]$	LDV Measured Q	% Error
1	220.4	7.5	8	125.2	1610	2.40	1664	3.35
2	220.6	22	15	155.6	1161	1.59	1100	5.25
3	220.5	21	15	125.4	1575	2.38	1650	4.76
4	220.8	11	15	219.4	2207	3.32	2300	4.21
5	220.8	40	15	255.3	3155	4.50	3121	1.08
6	220.8	21	17	225.6	2944	4.18	2900	1.49

Table 4.1: The dimensions and results from the ring-down measurement of a single point on the surface of a 220MHz AlN CMR. The quality factors as found through LDV measurements were all within 5.25% of the electrically determined Q, with higher Q devices having more better precision.

4.4 Measurement Error

From Appendix A.3 the out-of-plane measurement resolution of the LDV can be calculated to be 16pm. In practice, this error may be larger due to the reflectivity of the surface and the stability of the resonator motion itself but can also be reduced through extensive averaging. To determine the actual error associated with these measurements, a single point on a sample resonator was measured sequentially ten times. The results are shown in figure 4.8. The average displacement error over the entire ring-down event is 24.6pm. By fitting ring-down curves to this data, a minimum and maximum quality factor was found to be 1863 and 2009 respectively. This yields an error of $\pm 3.85\%$ in Q.

4.5 Future Work

This method could be applied to any bulk acoustic or flexural device that has a measurable out-of-plane motion component. Frequencies up to the 1.2 GHz limit of the UHF-120 could potentially be measured as well, by using smaller time samples and smaller delay steps. In addition to quality factor, this measurement method could be

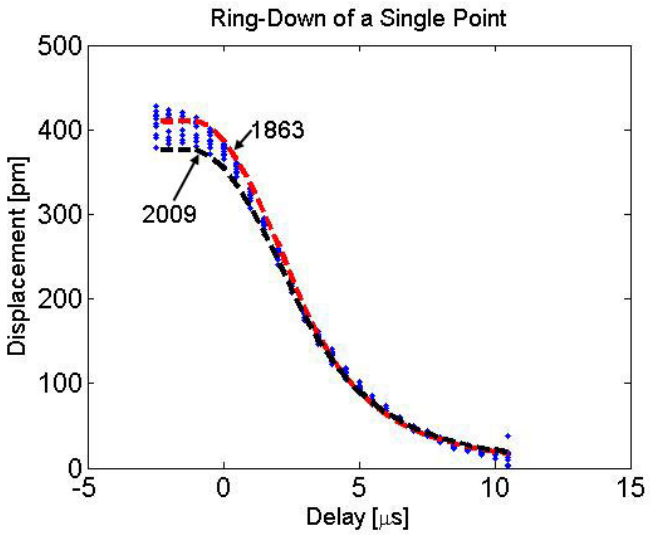

Figure 4.8: To determine the error associated with these measurements, a single point was measured ten times and a ring-down curve was fit to the two extremes. A total error of $\pm 3.85\%$ in Q was found.

used to determine the presence of non-linearities in the device and it could potentially be used to measure the onset of parametric resonance at previously unachievable frequencies [48].

Chapter 5

Measuring Spatial Wavelengths on the Surface of a CMR

5.1 Background

The surface of an ideal contour-mode resonator (CMR) would oscillate with a single uniform wavelength, however, due to the fact that multiple materials are used in its construction, the motion at the surface of the CMR is a superposition of multiple wavelengths. Aluminum, aluminum nitride, and platinum, the typical materials used in the devices each have a unique acoustic velocity that is governed by their densities and Young's moduli. The resulting wavelength for each material is defined by

$$\lambda = \frac{1}{2\pi f_0}\sqrt{\frac{E}{\rho}} \tag{5.1}$$

where f_0 is the resonant frequency, and E and ρ are the elastic modulus and density, respectively. At 220MHz and using standard values for the density and elastic moduli the resulting wavelengths for the materials used in the tested devices are shown below

in table 5.1. As described in section 2.2, the contour-mode resonant frequency of the device is set by the electrode spacing and is the result of the contribution of each of the material layers to the average acoustic wavelength of the resonator.

We are interested in determining the relative magnitudes for each of these wavelengths. These values can not be measured electrically but will be important in chapter 6 for measuring the ring-down of each of the materials in the resonator. This chapter develops the procedure for extracting the portion of the surface motion due to each material present in the 220MHz aluminum nitride piezoelectric CMRs similar to those used in the previous chapter.

Material	Elastic Modulus [GPa]	Density $[\frac{kg}{m^3}]$	$\lambda[\mu m]$
AlN	380	3200	49.5
Al	68.5	2700	22.9
Pt	168	21450	12.7

Table 5.1: The Young's modulus, density, and resulting acoustic wavelengths at 220MHz for each of the materials used in the CMRs tested.

5.2 Experimental Procedure

To analyze these wavelengths, the UHF-120 laser Doppler vibrometer was used to measure points along the path shown in figure 5.1. The vibrometer measured 180 points along the body of the resonator providing a spatial resolution of 733nm. The bandwidth was 2GHz with 128,000 FFT lines. At 220MHz the out-of-plane measurement resolution is approximately 15pm ±1.8pm as described in Appendix A.3. The device was driven at its resonant frequency which was determined by electrical admittance data using the same method as described in section 4.3. The devices were driven at -3dBm.

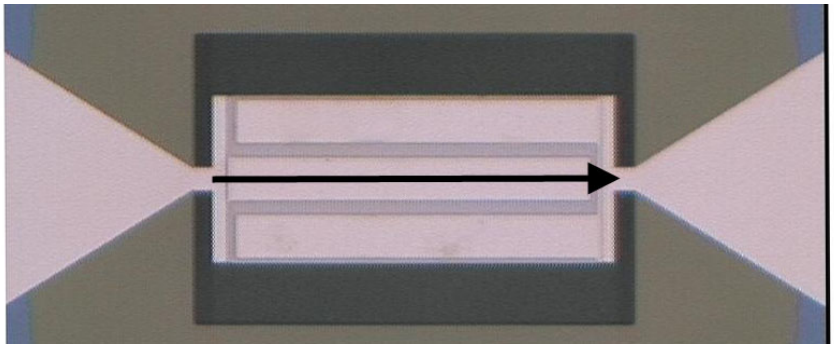

Figure 5.1: The surface of the resonator was scanned along the path shown. The spatial resolution was increased to 733nm to reduce the measurement time.

The magnitude and phase data gathered at each point can be combined using

$$z(t) = (\text{Magnitude}) \cdot \sin(\omega t + \text{phase}) \tag{5.2}$$

to produce a two-dimensional mode shape of the surface of the resonator as shown in figure 5.2. As described before, the mode shape is not composed of a single wavelength, but rather a superposition of multiple wavelengths. To determine these wavelengths, a spatial FFT of this mode shape was then taken to determine the magnitudes of each of the dominant wavelengths (figure 5.3). The peaks at approximately $15\mu m$, $25\mu m$, $54\mu m$ are associated with the Pt, Al, and AlN layers respectively. The mismatch with the values in table 5.1 are due to variations in the densities and moduli in the experimental devices as compared to the standard values.

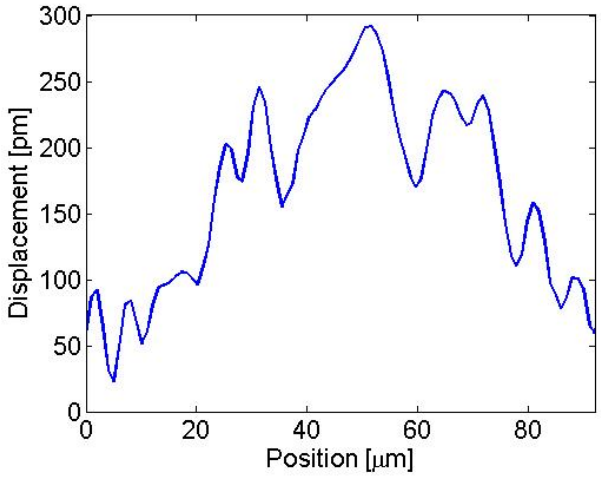

Figure 5.2: The mode shape along the centerline of a 220MHz resonator. As is evident, the mode shape is a superposition of multiple wavelengths due to the different material properties of each layer.

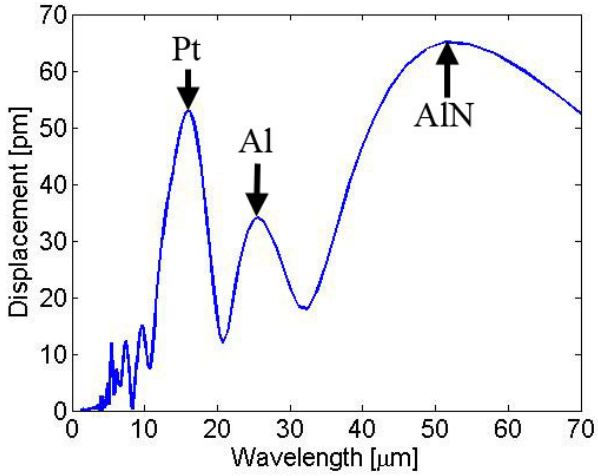

Figure 5.3: The spatial FFT of the surface of the resonator produced by the mode shape. There are peaks at $15\mu m$, $25\mu m$, $54\mu m$. Variations in the stiffness and density would account for the variations in wavelength with respect to the analytical values.

Chapter 6

Measuring Ring-Down For Each Material

6.1 Introduction

We are interested in measuring the ring-down time and therefore the energy dissipation of each of the material layers that compose the contour-mode resonator (CMR) using laser Doppler vibrometry (LDV). This time constant would be indicative of the energy lost due to intrinsic material losses and interfacial dissipation between two adjacent layers. To do this requires a combination of the measurement techniques described in the previous two chapters. We are interested in determining how the FFT peaks associated with each material decay over time after the actuation signal is removed. By doing so, we can determine the time constant for the exponential decay in motion for each of the materials.

6.2 Experimental Procedure

A ring-down measurement is performed at each point along the path shown in figure 5.1. This provides a portrait of how the two dimensional mode shape from chapter 5 decays after the drive signal is cut-off. At each time point a spatial FFT is performed on the mode shape and the magnitude of each peak is obtained. From this the ring-down profile for each of the peaks in the spatial FFT can be plotted. Figure 6.1 shows the ring-down profiles for each of the materials in a 220MHz CMR. A curve has also been fitted to the experimental data as described in chapter 4. Quality factor is typically a measurement of the energy loss of the resonator as a whole, but for clarity the effective quality factor for each material has been calculated as a way of understanding the energy loss of each layer.

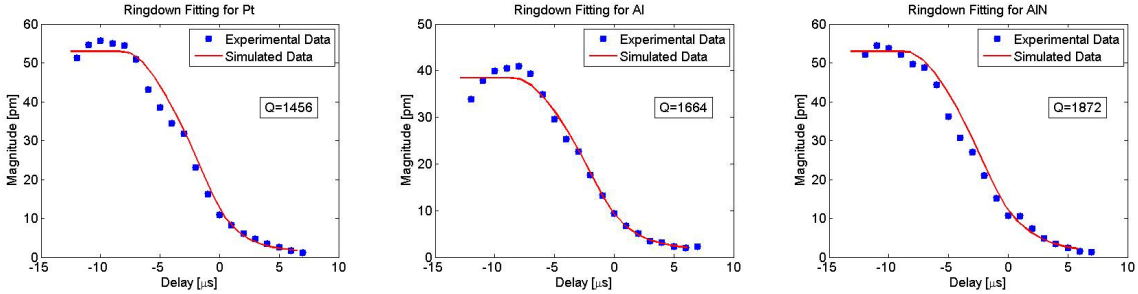

Figure 6.1: The ring-down profile of the three peaks in the spatial FFT associated with Pt(a), Al(b), AlN(c). Each material shows a unique time constant i.e. quality factor. Further experimental work will be conducted to better understand these effects.

6.3 Results and Discussion

Eight devices were tested for this study. These include five devices with a $1\mu m$ aluminum nitride layer and three devices with a $1.5\mu m$ aluminum nitride layer. Each device had identical body dimensions ($100\mu m$ long x $54\mu m$ wide). The dimensions of the anchors varied in each case. Electrical data was collected using a Rhode&Schwarz ZVL

Table 6.1: The resonant frequency, Q, anchor dimensions, and the bus bar width of the devices tested. Two thicknesses of AlN active layers were tested.

Device #	AlN Thickness [μm]	f_0 [MHz]	Electrical Q	Anchor Length [μm]	Anchor Width [μm]	Busbar Width [μm]
1	1.0	218.58	1161	21	15	6.59
2	1.0	220.53	1505	21	15	7.33
3	1.0	220.75	2207	11	15	6.96
4	1.0	220.78	3155	40	15	7.33
5	1.0	220.49	2914	11	15	6.96
6	1.5	232.65	1360	21	15	7.33
7	1.5	232.28	1708	11	15	6.96
8	1.5	233.14	2101	40	15	7.33

network analyzer. From this, the resonant frequency and electrical quality factor were extracted for each device. Table 6.1 shows these values and the dimensional values of each resonator (figure 6.2).

Figure 6.3 shows the results from measuring the five 220MHz devices with a $1\mu m$ aluminum nitride layer. For clarity a dashed line has been drawn along a 1:1 line between the X and Y axes. This line would represent the position where the effective material Q matches the device electrical Q. For each device, the effective material quality factor for aluminum nitride follows this line with an R^2 value of .987. Intuitively this is the result of the fact that it is the aluminum nitride layer that is generating the electrical response, through the Piezoelectric effect, that is creating the device electrical Q. If the aluminum nitride layer is oscillating, it is generating strain and therefore an electrical response. The effective Q values for aluminum and platinum also follow linear trend lines similar to aluminum nitride. For each device, platinum has an effective Q that is, on average, 11.3% lower than aluminum nitride. This indicates that there is more energy dissipation in the platinum layer than in the aluminum nitride layer. With these measurements, it is not possible to parse out whether these losses come from intrinsic material losses in

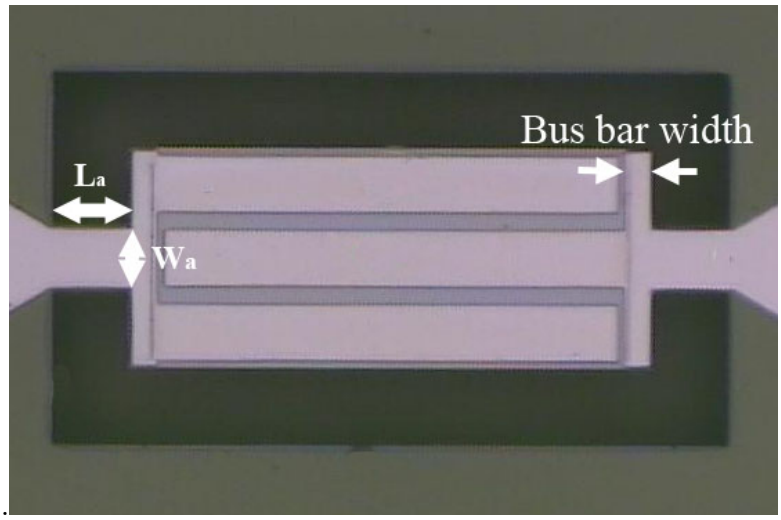

Figure 6.2: The length, L_a, of the anchors of CMRs below 220MHz has a significant impact on performance. It was shown that Q could have a five-fold variation due to anchor length. No correlation between the width, W_a, of the anchors and Q was found.

the platinum or if they are the result of interfacial losses at the aluminum nitride and platinum interface. A similar trend is seen with the aluminum layer except that it has, on average, an effective Q that is 13.6% lower than the aluminum nitride layer.

Figure 6.3 shows the results from measuring the three 220MHz devices with a $1.5\mu m$ aluminum nitride layer. The trend is similar to that of the devices with the thinner aluminum nitride layer. The effective material quality factor of the aluminum nitride layer matched the electrically measured Q. In this case the effective quality factor values for the platinum layers are much closer in value to the aluminum nitride layer. The platinum Q values are only 4% less than the aluminum nitride layer. The values for the platinum layer are within 12% is similar to the $1\mu m$ devices.

6.4 Conclusion

A new method has been developed for measuring energy losses associated with the individual layers of a resonant structure. By using a newly developed technique for

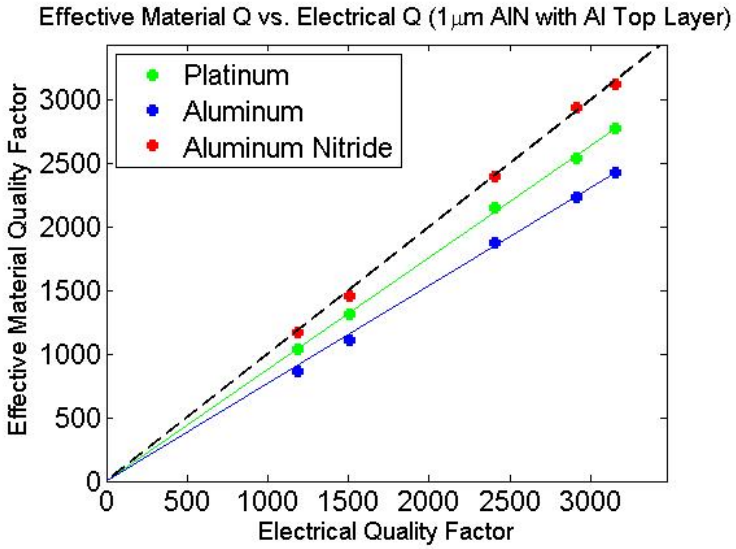

Figure 6.3: The electrically measured device Q vs. the effective material quality factors for each material layer of the five devices fabricated with a $1\mu m$ aluminum nitride layer.

measuring ring-downs of an ultra high frequency resonator it is possible to study the energy loss of any material on the device that possesses a unique acoustic wavelength. Eight devices were tested with device quality factors ranging from less than 1200 to almost 3200. In each case, it was possible to extract the effective material quality factor for each of the layers of the CMR. The effective material quality factor for the aluminum nitride layer closely matched the devices electrical quality factor, whereas the effective Q for the aluminum and platinum layers were lower by 13.6% and 11.3% respectively for the $1.5\mu m$ aluminum nitride devices and 12% and 4% respectively for the $1\mu m$ devices. The increased loss in the aluminum layer occurs even though there is less coverage of this layer versus the bottom platinum layer that covers the entire resonator. These measurements support the theory discussed in [49] that aluminum nitride is a relatively high-Q material and it is the metal electrodes that are responsible for low Q values. The aluminum layer is more lossy than the platinum layer so higher performance could be gained by fabricating

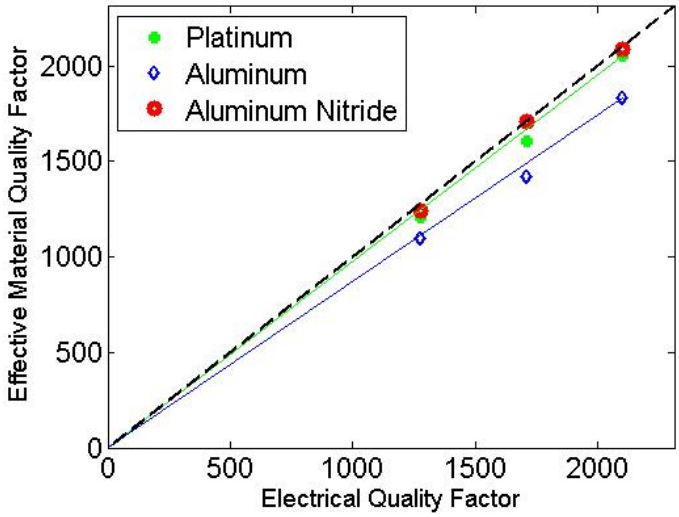

Figure 6.4: The electrically measured device Q vs. the effective material quality factors for each material layer of the five devices fabricated with a $1.5\mu m$ aluminum nitride layer.

the devices using platinum for the upper and bottom metal layers.

6.5 Future Work

Future work for this study should include measurements on similar CMRs with other metal layers. It would be useful to study devices that had identical physical dimensions but with alternative metals such as silver or gold. This could provide better insight into which materials produce the least energy loss. In addition, other types of resonant devices could be tested. It would be useful to measure a multi-layer flexural device such as a Piezo-electrically fixed-fixed beam.

Appendix A

Laser Doppler Vibrometery

A.1 Theory

One of the leading methods for non-contact displacement measurements of MEMS devices is through the use of laser Doppler vibrometery. This was first employed on the macro-scale in 1964 for measurements in flow fields using a homodyne interferometer [50]. With the advent of the heterodyne interferometer [51] laser Doppler Vibrometry (LDV) could be employed in more practical applications due to its ability to measure much smaller frequency shifts as well as making it more robust to environmental conditions. This method, as well as the sources of error and these values associated with the Polytec UHF-120 used in this thesis are described below. Current technology allows LDV measurements from DC to 1.2GHz with a noise floor of 4pm and with sub-picometer resolution [52].

Figure A.1 shows the laser light path of a typical heterodyne LDV. Coherent light is produced by, in the case of the UHF-120, a NdYAG-crystal laser. The beam is split, using a beam splitter, into a reference beam and a measurement beam. The measurement beam passes directly through another beam splitter, through the object lens and then strikes the surface of the DUT. The reference beam is passed through a Bragg cell which shifts the beam frequency up by 40MHz. After the measurement beam reflects off of the surface of the DUT it returns through the objective and is then redirected by the beam splitter toward a photo-detector. The measurement beam and the reference beam are mixed together at a final beam splitter just before the photo-detector. Because the interferometer measures the reflected light along the same axis as the illuminated light, the measurement can be modeled as a one-dimensional wave equation [53]:

$$\frac{\partial^2 E(x,t)}{\partial x^2} = \frac{1}{c_m^2(x,t)} \frac{\partial E(x,t)}{\partial t} \tag{A.1}$$

where $x = 0$,and $c_m(x,t) = c/n(x,t)$ is the speed of light in a medium of index of refraction, $n(x,t)$. By assuming that the index of refraction is constant, the solution at

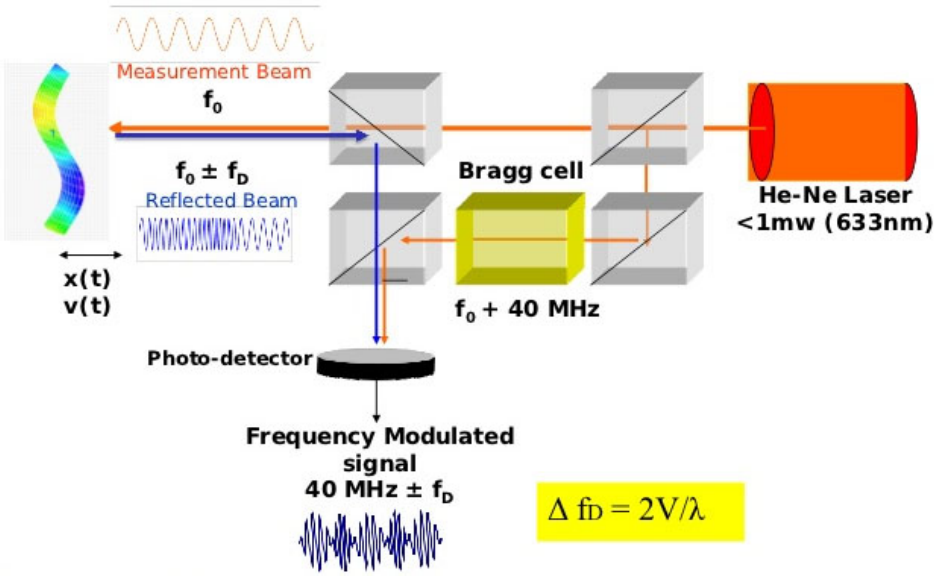

Figure A.1: A schematic of the light paths of a heterodyne laser Doppler vibrometer and its various components.

the surface of the DUT, $s(t)$ is:

$$E_s(s(t), t) = E_0 cos(\omega t - k(s(t))) \tag{A.2}$$

where ω is the frequency of the laser source, E_0 is the emission power of the laser and $k = 2\pi/\lambda$, is the wavenumber with λ being the wavelength of light. Using several simplifications the electric field at the detector is:

$$E_d(s_d, t) = \sqrt{r} E_0 cos(\omega t - \phi(t)) \tag{A.3}$$

where r is the reflectivity of the DUT, and $\phi(t)$ is defined by:

$$\phi(t) = (ks_d - 2ks(t) - 2ks_0) \tag{A.4}$$

The first term in equation A.4 represents the distance from the sample to the detector. The second term refers to the surface motion of the DUT and the third term is the average distance from the laser to the DUT. The Doppler shift is given by

$$\frac{d\phi(t)}{dt} = \frac{d(kn(2s(t) + 2s_0 - s_d))}{dt} = k\frac{d(OPL(t))}{dt} \tag{A.5}$$

where OPL is the total optical path length. The Doppler shift is therefore a result of the change in the path length with respect to time, i.e. the velocity of the surface of the DUT. The resulting light energy from the measurement beam that is incident on the

photo-detector is therefore:

$$E_d(s_d, t) = \sqrt{r}E_0 cos(\omega t + 2knv(t)) \tag{A.6}$$

where n is simply the number of integer wavelengths along the light path. The total light that is incident upon the detector is the sum of this measurement beam and the reference beam which has a similar equation except with a fixed phase for the reference beam

$$E_d(t) = E_m cos(\omega_1 t - \phi(t)) + E_r cos(\omega_2 t - \phi_0), \tag{A.7}$$

where $E_m = \sqrt{r}E_0$ is the amplitude of the measurement beam and E_r is the amplitude of the reference beam. The detector outputs a current which is proportional to the square of the electric field. The electric current can be found to be

$$i_p = K[P_m + P_r + 2\sqrt{P_m P_r} cos(\omega_1 t - \omega_2 t - \phi(t) + \phi_0)] \tag{A.8}$$

where P_m and P_r are the optical powers of the measurement and reference beam respectively and K is the linear amplification of the photo-detector. The purpose of the Bragg cell is to shift the reference beam frequency by ω_c. The result is that $\omega_c =\mid \omega_1 - \omega_2 \mid$ and equation A.8 becomes

$$i_p = K[P_m + P_r + 2\kappa\sqrt{P_m P_r} cos(\omega_c t - \phi(t) + \phi_0)] \tag{A.9}$$

where κ is defined as a heterodying efficiency that accounts for any loss of signal through the Bragg cell [53]. Something to note is that the actual Doppler frequency shift of the light that has been reflected off of the surface of the DUT is very slight. It can be shown that the actual frequency shift, Δf, is

$$\Delta f \approx \frac{v_s}{c} \tag{A.10}$$

where v_s is the velocity of the DUT surface and c is the speed of light. At 220MHz with a displacement of 300pm, the maximum velocity of the surface $400\frac{mm}{s}$. At this velocity, the frequency shift is $1.4 \times 10^{-9} Hz$. Because of this, the LDV doesn't technically measure a Doppler shift but rather the time-dependent phase changes between the reference and measurement beams.

A.2 Averaging

Measured data from any source is always a superposition of some amount of noise. To minimize this noise and thereby improve the signal to noise ratio, averaging is applied to the signal. The LDV captures a time domain sample and has the ability to convert it into an FFT in the frequency domain. Averaging can be applied in either domain and the two most common methods for averaging LDV data in the frequency domain is magnitude

and complex averaging. Since this thesis focuses on averaging in the frequency domain the focus of this section will be on magnitude and complex averaging.

To perform averaging in the frequency domain, a series of time traces are collected and an FFT is performed on each of these time samples independently. The time samples must be the same length so that each of their respective FFTs has the same number of lines. In addition, if the data collected is not in steady state, each sample should be taken from the same point in the transient event. This can be accomplished by synchronizing the transient event and the measurement by means of a trigger.

When an FFT is taken of a single time measurement, each bin is represented by a phasor S_n. These complex values represent the magnitude and phase of each of the frequency components that make up the time signal.

A.2.1 Magnitude Averaging

When magnitude averaging is applied, the phasor for each of the bins in the FFT is summed with the corresponding phasor from each time sample, the magnitude is then taken and the result is divided by the number of time samples,

$$|\bar{S}| = \frac{1}{N}\sum_{n=1}^{N}|S_n| \tag{A.11}$$

where N is the number of time samples taken. Magnitude averaging results in a higher noise floor due to the fact that incoherent or non-phase-locked noise will not be eliminated. Magnitude averaging is useful when it is not possible to maintain a steady phase value between the input and output signal such as when measuring the frequency response using only Brownian motion. If there is no drive signal available magnitude averaging is the best averaging method.

A.2.2 Complex Averaging

When complex averaging is used, the phasor from each frequency bin in the FFT is split into its real and imaginary portions. Each portion is then averaged independently,

$$\bar{S} = \frac{1}{N}\left(\sum_{n=1}^{N} Re(S_n) + i\cdot\sum_{n=1}^{N} Im(S_n)\right) \tag{A.12}$$

complex averaging is very effective at removing noise due to the fact that, for each FFT bin, the phase value for the incoherent noise is random with respect to the drive signal and will therefore be averaged away over successive measurement averages. To make use of complex averaging it is necessary to provide a drive signal or some other reference that can be used to phase-lock the desired output signal. This ensures that the desired signal is not averaged away in the same manner as the noise.

A.3 Resolution

Polytec specifies the amplitude resolution of the UHF-120 as a function of resolution bandwidth (RBW) in Hz. The RBW is a function of the measurement bandwidth selected as well as the number of FFT lines chosen for the measurement. For a given bandwidth, BW the sampling frequency, f_s is

$$f_s = 2.56 \cdot BW \tag{A.13}$$

The sample time, t_s, is then found by

$$t_s = \frac{N_{fft}}{BW} \tag{A.14}$$

Where N_{fft} is the number of FFT lines selected. From here the resolution bandwidth is,

$$RBW = \frac{1}{t_s} \tag{A.15}$$

Finally, the displacement amplitude resolution is

$$DisplacementAmplitudeResolution = \frac{30 \times 10^{-15} m}{\sqrt{Hz}} \cdot RBW \tag{A.16}$$

As an example, for the settings used in chapter 4.5, a bandwidth of 2GHz with 6400 FFT lines, the RBW is 312.5kHz. This would give a displacement amplitude resolution of 16.8pm. With repeated averaging, however, this value can be lowered into the sub-picometer range.

Appendix B

Automation of the Polytec UHF-120 LDV

In its off-the-shelf form, the Polytec UHF-120 is a single point system. It is intended to take a single measurement at a single spatial point and at a single drive frequency and power setting. The measurements taken in this thesis include, in some cases, thousands of measurements at different spatial points and drive settings. To this end, it was necessary to automate the measurement process so that the experiments could be performed quickly and effectively.To automate this process, Mathworks Matlab was used in conjunction with its graphical user interface (GUI) coding plug-in. This allowed for the development of an easy to use working environment for the large number of measurements required for these studies.

Figure B.1 shows the hardware components required and their associated connections. The components include:

- UHF-120 interferometer head
- LeCroy fast digitizing oscilloscope
- Polytec PC
- Rhode&Schwarz function generator (FGN)
- Motion control hardware

The following sections describe each of the hardware components necessary for the automation of the LDV measurements.

B.1 Spatial Automation

The UHF-120 interferometer head was placed onto a two axis motion control stage to move the laser in the X and Y axes with respect to the DUT. A stepper motor

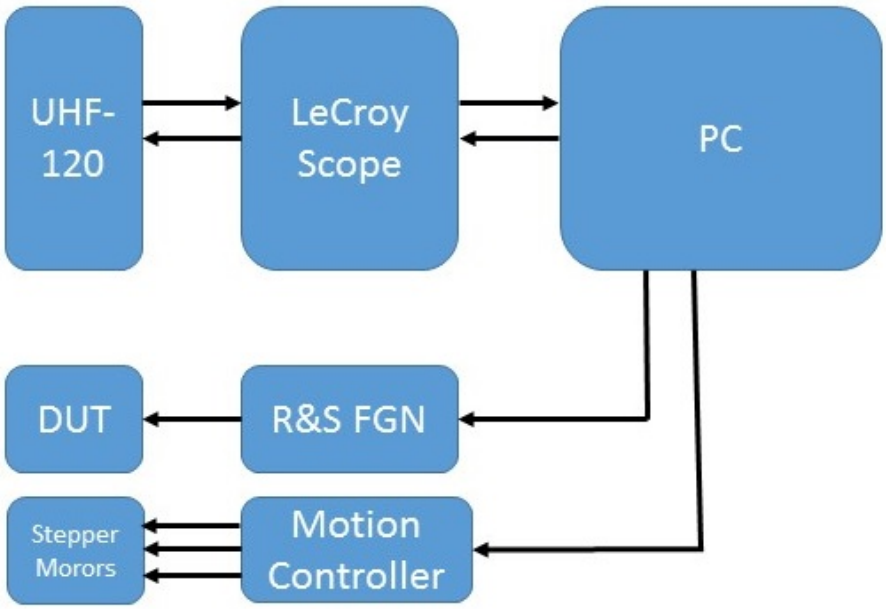

..

Figure B.1: The hardware and associated connections involved in automating the LDV measurement process, The PC running a Matlab GUI controls all functions and collects the data.

was also mounted onto the focus system to allow automated focusing (figure B.3). Each stepper motor was controlled by a Parker Motion ViX500IM stepper drive which received commands through the serial port of the PC. The Matlab GUI, known as GibSoft, controls the stepper drives through the COM ports on the PC (figure B.2).

To control the spatial positioning in the in-plane, or X-Y, directions, image tracking was required. Before running GibSoft the user must run a setup GUI, known as VibSetup (figureB.4). The video feed from the LDV is digitized and displayed in a preview window within the VibSetup GUI. The user must first select a fiducial. This is a region of the image that the image correlation algorithm can use to track the position of the DUT within the image. The user can then select the desired scan points. There is an option of a single point, a line or a box of measurement points. For the latter two choices, the density of points can be selected. Once the spatial points have been selected, the files should be saved and then the user must open GibSoft and load the setup file created in VibSetup. A built-in function called `normxcorr2`, is used to match the position of the fiducial within the live video feed. This function outputs the position of the lower left corner of the fiducial within the live image which can then be used to align the DUT under the vibrometer with an accuracy of approximately 400nm.

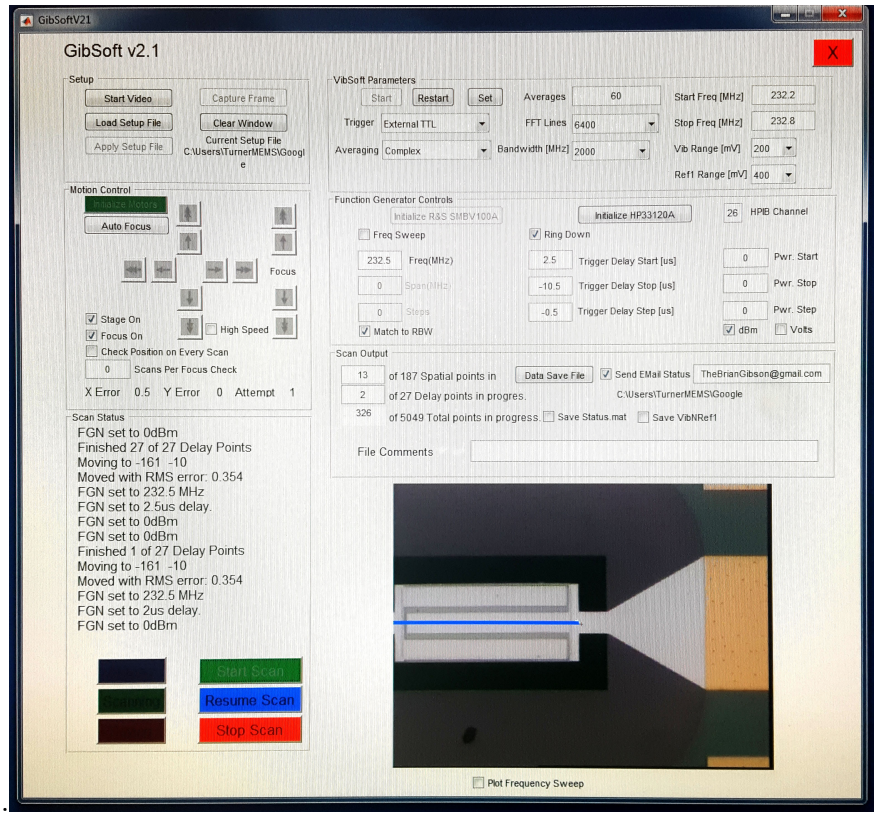

Figure B.2: The graphical user interface developed to automate the LDV measurements of the UHF-120. Through this interface, the user can select all of the measurement parameters for standard or ring-down measurements. Once the scan is started, no input is needed from the user and the software will email the user once the measurements are complete.

B.2 Setting Measurement Parameters

Polytec supplies software, known as VibSoft, to start and stop the LDV measurements as well as set the measurement parameters. These parameters include:

- Bandwidth
- Number of FFT lines
- FFT frequency range
- Vib and Reference channel sensitivity
- The type of averaging (complex or magnitude)
- The number of averages
- Triggering method and source

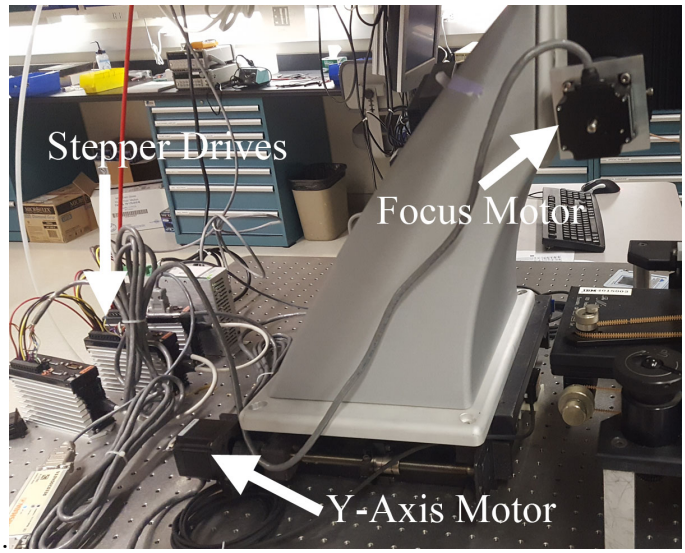

Figure B.3: The stepper motors used to drive the Y axis and focus. Also shown are the Parker Motion ViX500IM stepper drives. The X axis motor is not visible.

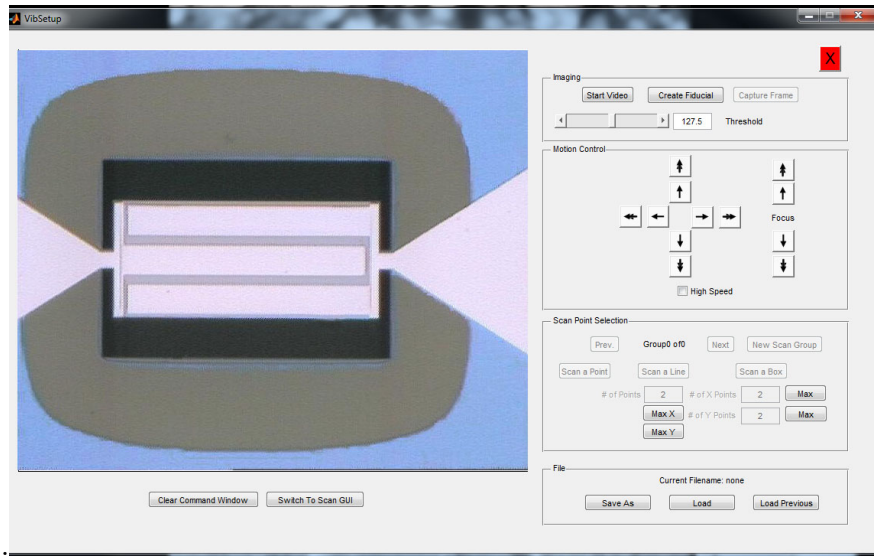

Figure B.4: The VibSetup GUI used to define the spatial measurement points. The user first selects a fiducial area which is used by GibSoft to track the DUT within the objective area. The desired scan points can then be selected.

GibSoft allows the user to input all of these settings into the GUI and, through an ActiveX portal, GibSoft sets these parameters automatically in VibSoft. This allows a single interface for the user to work with.

The next step is to select whether to perform a ring-down measurement or a parameter sweep such as a frequency or power sweep. If the user chooses a parameter sweep such as frequency, the frequency center, span and number of steps can be entered. GibSoft

connects to the function generator (FGN) through a LAN connection to control the frequency and power settings. For a ring-down measurement, the user must select a frequency and power setting and then select the range of measurement delays and steps overwhich to perform the measurement.

B.3 Data Acquistion

VibSoft acquires the data from UHF-120 vibrometer head using a LeCroy fast digitizing oscilliscope. The data is then transferred to the PC via a LAN connection. VibSoft then provides the following post-processing capabilities:

- Display of measurement and reference time traces
- Display of FFT of measurement and reference signals
- Application of complex and magnitude averaging to the time or frequency based data

Through VibSoft, GibSoft initiates the measurement, waits for the measurement to finish, and then pulls the desired data. This data is stored in a temporary file while the scan is being performed. Once all of the measurements are completed, this data along with all of the measurement parameters, are saved to a user-defined file name and location. The output data includes:

- Vib channel displacement magnitude
- Vib channel phase
- Vib channel frequency
- Reference channel voltage
- Delay
- X axis position
- Y axis position
- X axis error
- Y axis error
- A time stamp for each measurement

The measurement parameters include:

- All vibrometer settings

- All function generator settings
- All spatial points
- All frequency, power and delay values
- An image of the DUT
- The name of the data file

All of these parameters would allow a user to recreate an experiment using only the output file. The length of time for each scan can take anywhere from a few seconds to several days depending on how many spatial, frequency, power, and delay points are chosen as well as how many averages are selected. Because the process is automated, no input is needed from the user during this time. The software can email the user when the measurements are completed.

B.4 In-Plane Spatial Error

There is in-plane spatial error when using GibSoft due to the image tracking system and the motion control system used to position the laser. The CCD used to image the device outputs in PAL format with a resolution of 576 horizontal pixels by 768 vertical pixels. All measurements are taken through a 50X objective lens and as a result the video resolution is 2.73 pixels per micron in the X and Y axes. Both Axes have the same resolution due to the fact that the aspect ratio of the image is rectangular and because each pixel is not square. Given this resolution, the maximum in-plane spatial precision is 366nm. In practice, the positioning error is higher due to the precision of the stepper motors used. Because the image tracking algorithm can register this error, an RMS value for the combined X and Y error is calculated by GibSoft and saved to the output file. Over five ring-down measurements taken during the experiments in chapter 6 the average error due to the stepper motors is 0.1625 pixels or 60nm. The combined error is then 426nm.

B.5 Future Work

Future work for GibSoft would include an improved motion control stage for better X-Y positioning. The spatial error could be reduced if, for instance, a piezo-electric actuator, was used in conjunction with the existing stepper motor/lead screw system. This would allow much greater precision in positioning as well as potentially reducing the time required to move from one position to the next. Moving spatial positions can consume as much as twenty seconds per measurement. When this is multiplied by several thousand points it becomes apparent how much time could be saved in this upgrade.

Another future project could involve bypassing the VibSoft software provided by Polytec. It is possible to control the fast digitizing oscilloscope directly with Matlab and this may further reduce the time required to make measurements. Additional research would need to be done to determine the usefulness of this work, since Polytec has, to some extent, optimized the interface between the oscilloscope and VibSoft.

An improved auto-focus algorithm would also serve to greatly reduce measurement times for GibSoft. It currently requires approximately thirty seconds to complete an autofocus cycle. This time is consumed by the built-in Matlab imaging script used to gauge focus as well as the focus algorithm written by this author. Both areas could see substantial improvement.

Appendix C

Phase Noise

An important characteristic in the design and implementation of an oscillator circuit is its noise level. Oscillator noise can be broken down into amplitude noise and phase noise. This section provides an explanation of both as well as sources of noise and what impact the resonator has on contributing to or reducing noise.

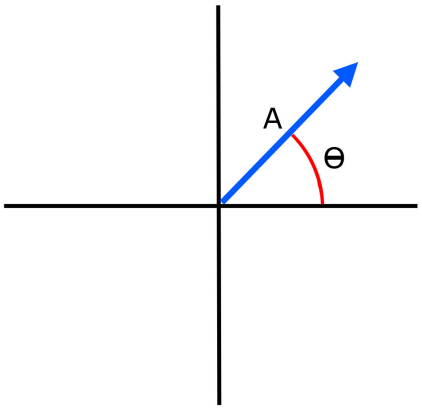

..

Figure C.1: The output of an oscillator circuit can be represented with a phasor diagram. An ideal oscillator would have a fixed amplitude, A, and phase angle, Θ.

The output of an oscillator circuit can be represented by a phasor (figure C.1) with a given amplitude, A, and phase, Θ. An ideal oscillator would have a fixed value for each component of the phasor. In practice, the phase and amplitude have some amount of random time variance(figure C.2). This variance is known as phase noise and amplitude noise.

In an oscillator circuit the amplitude of oscillation is controlled by non-linearities in the feedback circuit [54]. If there is any perturbation in the amplitude due to noise, the feedback circuit automatically suppresses it. As a result, amplitude noise is not usually a major problem in oscillator circuits. Of greater concern is phase noise. This is not easily

controlled by the feedback circuit and it comes from many sources.

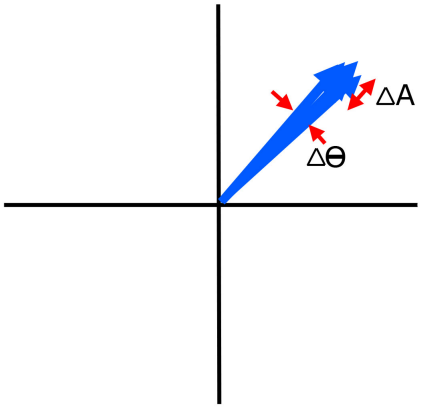

..

Figure C.2: In practice, oscillators have noise in both phase and magnitude directions.

On a power spectrum, an ideal oscillator would appear similar to a delta function with all energy occurring at a singular frequency. The presence of phase noise causes the signal energy to spread out into side bands adjacent to the main carrier frequency. An example of a phase noise plot is shown in figure C.3. Because of the symmetry above and below the center frequency, a phase noise diagram only shows the left side bands and assumes that the right side bands are identical. The units of magnitude are in $\frac{dBc}{Hz}$ because the y axis is normalized to the power of the center frequency. The unit, dBc represents decibels below the carrier. Noise at frequencies near the carrier is known as "close-in" phase noise whereas noise at frequencies much higher or lower then the carrier frequency is known as "far from carrier" phase noise. Far from carrier phase noise is typically white noise because it has zero slope on the phase noise plot and its amplitude is not related to frequency.

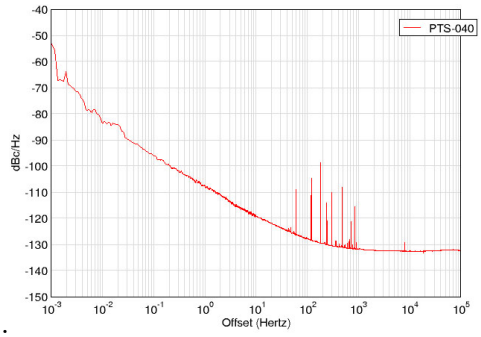

..

Figure C.3: An example of a phase noise diagram. Because of symmetry, only the left side of the power spectrum is shown. The Y-axis is in $\frac{dBc}{Hz}$ and is normalized to the power of the center frequency.

Some of the noise sources include thermal noise, shot noise and flicker noise. Thermal noise is caused by Brownian motion of the electrons in the electrical components as well as in the resonator [55, 56]. Shot noise is the result of the discreet nature of electron flow at very low current levels in the pn junctions of the amplifier elements and power supply. Flicker noise is related to the close-in phase noise and is found in all active electrical elements such as amplifiers and transistors in the oscillator circuit.

A common model for phase noise is the Leeson equation [57]

$$L(f_m) = 10log\left[\frac{1}{2}\left(\left(\frac{f_0}{2Qf_m}\right)^2 + 1\right)\left(\frac{f_c}{f_m} + 1\right)\left(\frac{FkT}{P_s}\right)\right] \tag{C.1}$$

where f_0 is the output frequency, f_m is the offset from the output frequency, f_c is the $1/f$ corner frequency, F is the noise factor of the amplifier, k is Boltzmann's constant, T is the temperature, and P_s is the output power. The first term in the brackets represents the contribution to the close-in phase noise, the second term represents the mid range noise known as $1/f^3$ noise and the last term is the white noise that is from carrier. The close-in phase noise is directly proportional to the Q of the resonator. A higher Q will produce less close-in phase noise.

Appendix D

Determining Q and K_t^2 from Admittance Data

D.0.1 Quality Factor

From the S_{11} parameters produced by the vector network analyzer, an admittance response plot from the resonator can be produced. The admittance data can be separated into real (conductance) and imaginary (susceptance) portions (figure D.1). From this data the quality factor, K_t^2 and other values can be extracted. There are four common methods for determining the quality factor from electrical admittance data. Each method is described below and, with quality data will provide identical results.

The real and imaginary portions of admittance form a phasor. The angle of that phasor as a function of frequency is often plotted along with the magnitude of the phasor. At resonance the slope of the phase data can be used to determine Q. The slope of the phase at resonance multiplied by the resonant frequency defines Q

$$Q = f_0 \cdot \frac{\partial \Phi}{\partial f} \tag{D.1}$$

where Φ is the phase at a given frequency, f.

The next method for determining Q is by measuring the resonance and anti-resonance peaks on the susceptance plot. Q is proportional to the difference between the resonance, f_r, and antiresonance, f_a peaks,

$$Q = \frac{f_0}{f_a - f_r} \tag{D.2}$$

The third method for determining Q is known as the "half power" method. If the magnitude of the admittance is plotted on the dB scale as shown in figure D.4, the bandwidth of the response at 3dB below resonance can be found.

$$Q = \frac{f_0}{\Delta f_{-3dB}} \tag{D.3}$$

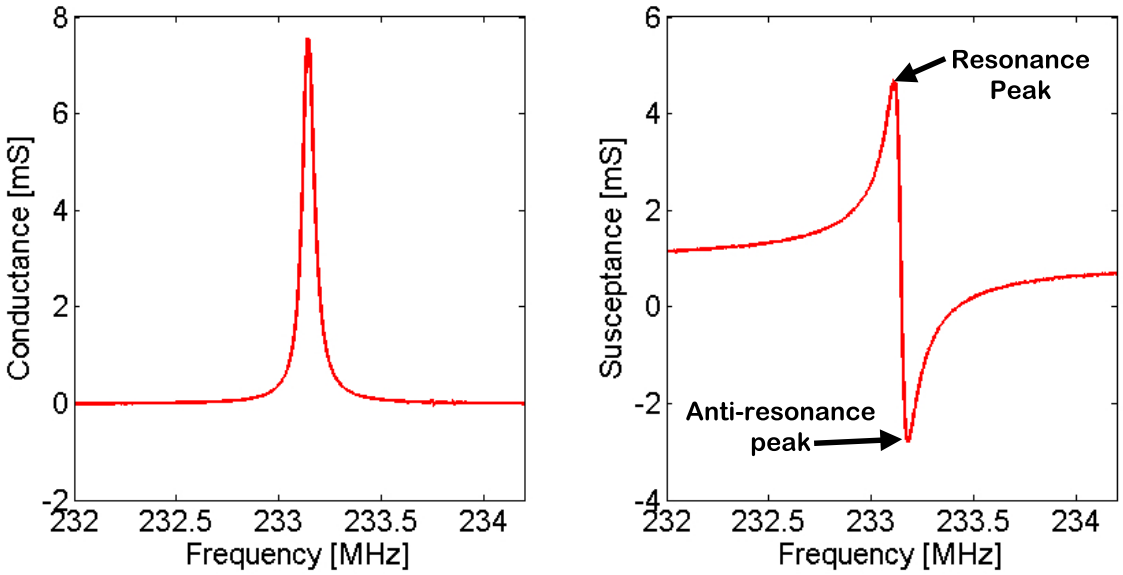

Figure D.1: The conductance and susceptance portions of admittance data generated by the VNA from a CMR. These represent the real and imaginary portions of admittance respectively.

The fourth and final method for determining Q is through curve fitting. A common model for a contour-mode resonator is known as the Modified Butterworth-Van Dyke model [58]. This modified version of the traditional Butterworth-Van Dyke model accounts for parastic capacitance, C_0, and resistance, R_0. Using this model, the equation for admittance $Y_{eq}(\omega)$ becomes

$$Y_{eq}(\omega) = \frac{1}{R_m + j\omega L_m + \frac{1}{j\omega C_m}} + \left(\frac{1}{j\omega C_0} + R_0\right)^{-1} + \frac{1}{R_{0p}} \tag{D.4}$$

Once a good fit is obtained, the value for Q can be found by

$$Q = \frac{1}{R_m} \cdot \sqrt{\frac{L_m}{C_m}} \tag{D.5}$$

and k_t^2 is found by

$$k_t^2 = \frac{\pi^2}{8} \cdot \frac{C_m}{C_0} \tag{D.6}$$

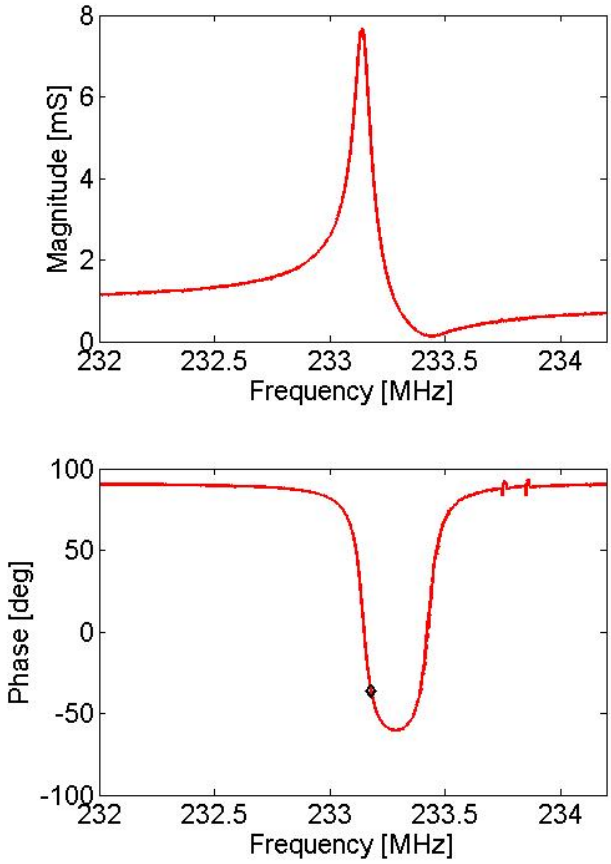

..

Figure D.2: The admittance data of a 220MHz AlN CMR in magnitude/phase form.

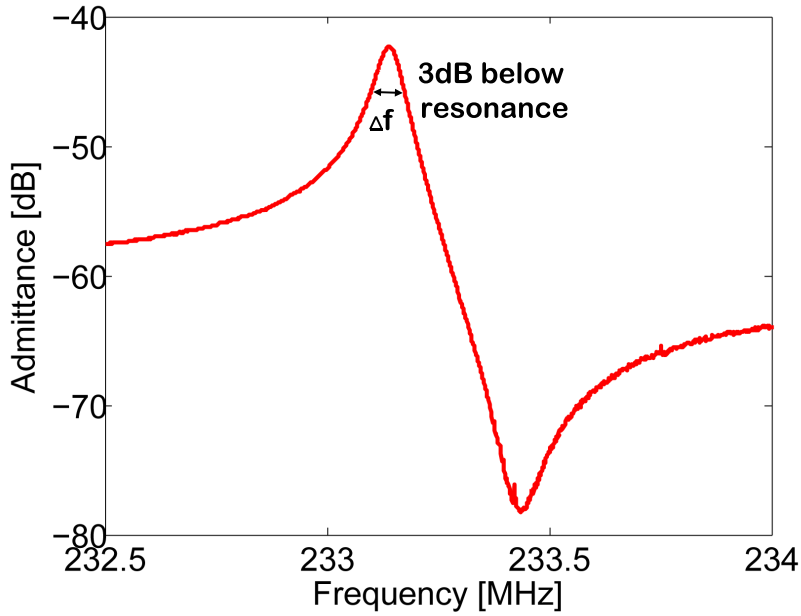

Figure D.3: The magnitude of admittance on a log scale of a CMR. The quality factor is the ratio between the resonant frequency and the 3dB bandwidth.

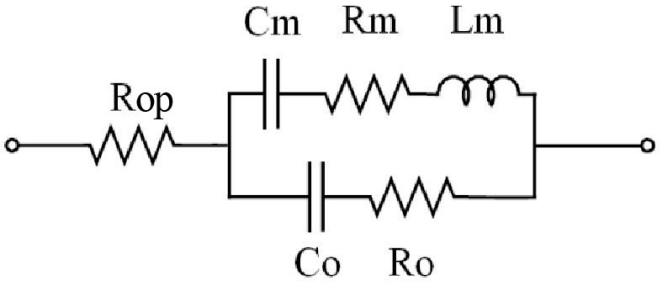

Figure D.4: The Modified Butterworth-Van Dyke model used for fitting the electrical parameters to the admittance data.

Appendix E

Transmission Line Theory

Traditional circuit analysis assumes that the physical dimensions of the electrical circuit to be analyzed is much smaller than the wavelength of the electrical signal. In contrast, transmission line theory takes into account the fact that the circuit is a substantial fraction of the electrical wavelength or multiple wavelengths long. Because the dimensions of the resonators used in this thesis are several acoustic wavelengths long, it is useful to use transmission line theory in studying the behavior of the acoustic energy that is escaping the active region of the device. Transmission line theory accounts for the propagation of waves along a medium and also provides tools to account for electrical (or, in this case, acoustic) reflections at an interface (the edge of the released region). This section provides a short tutorial on transmission line theory as it relates to the analysis in this thesis.

As shown in [59], a simple transmission line shown in figure(E.1)a can be broken into differential elements of length Δz. Each of these elements can be treated as a lumped model (figure E.1b) with a:

- Resistance per unit length, R, due to the finite conductivity of the material.
- Inductance per unit length, L, due to self inductance of the two conductors.
- Shunt conductance per unit length, G, due to dielectric losses.
- Shunt capacitance per unit length, C, due to the proximity of the two conductors.

By taking the limit as $\Delta z \to 0$, the voltage and current at any point can be given by

$$\frac{\partial v(z,t)}{\partial z} = -Ri(z,t) - L\frac{\partial i(z,t)}{\partial t} \tag{E.1a}$$

$$\frac{\partial i(z,t)}{\partial z} = -Gv(z,t) - C\frac{\partial v(z,t)}{\partial t} \tag{E.1b}$$

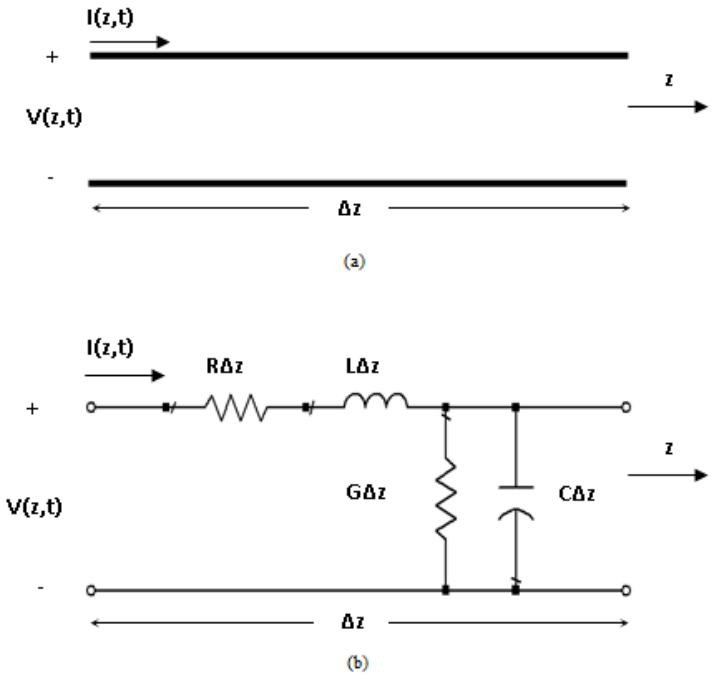

Figure E.1: A transmission line (a) can be analyzed as a cascade of lumped models (b) each with differential length Δz.

Equations E.1a&b are known as the telegraphers equations. If we are interested in the voltage and current only at steady-state, these can be simplified to

$$\frac{dV(z)}{dz} = -(R + j\omega L)I(z) \tag{E.2a}$$

$$\frac{dI(z)}{dz} = -(G + j\omega C)V(z) \tag{E.2b}$$

The solutions to E.2a&b can be solved to produce traveling wave equations for each

$$V(z) = V_0^+ e^{-\gamma z} + V_0^- e^{-\gamma z} \tag{E.3a}$$

$$I(z) = I_0^+ e^{-\gamma z} + I_0^- e^{-\gamma z} \tag{E.3b}$$

where

$$\gamma = \sqrt{(R + j\omega L)(G + j\omega C)} \tag{E.4}$$

and $e^{-\gamma z}$ represents wave propagation in the -z direction and $e^{\gamma z}$ represents wave propagation in the z direction. If E.2a is combined with E.3a the characteristic impedance, Z_0 is given by

$$Z_0 = \frac{R + j\omega L}{\gamma} \tag{E.5}$$

If we assume that the transmission line is lossless ($R = G = 0$), which is an acceptable simplification for our analysis, then it can be shown that

$$Z_0 = \sqrt{\frac{L}{C}} \tag{E.6}$$

and equations E.3 can be rewritten as

$$V(z) = V_0^+ e^{-j\beta z} + V_0^- e^{j\beta z} \tag{E.7a}$$

$$I(z) = \frac{V_0^+}{Z_0} e^{-j\beta z} + \frac{V_0^-}{Z_0} e^{j\beta z} \tag{E.7b}$$

where

$$\beta = \omega\sqrt{LC} \tag{E.8}$$

Figure E.2 shows a transmission line that has been terminated with some load of im-

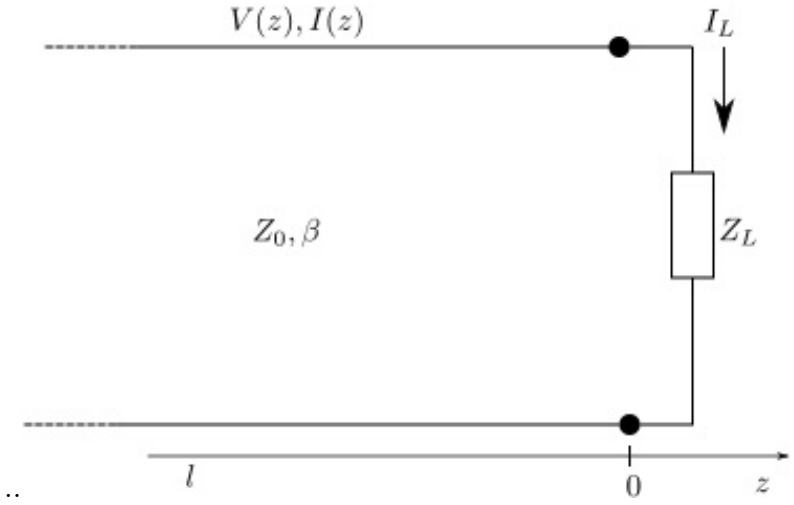

Figure E.2: A transmission line terminated with a load impedance.

pendance, Z_L. At the load ($z = 0$) the impedance is

$$Z_L = \frac{V(0)}{I(0)} = \frac{V_0^+ + V_0^-}{V_0^+ - V_0^-} Z_0 \tag{E.9}$$

Solving for the voltage reflected back into the transmission line from the load, V_0^-, gives

$$V_0^- = \frac{Z_L - Z_0}{Z_L + Z_0} V_0^+ \tag{E.10}$$

This yields a voltage reflection coefficient, Γ, given by

$$\Gamma = \frac{Z_L - Z_0}{Z_L + Z_0} \tag{E.11}$$

Equations E.7 then become

$$V(z) = V_0^+[e^{-j\beta z} + \Gamma e^{j\beta z}] \tag{E.12a}$$

$$I(z) = \frac{V_0^+}{Z_0}[e^{-j\beta z} - \Gamma e^{j\beta z}] \tag{E.12b}$$

For the purposes of this thesis, a special case is considered where the load impedence is an open circuit and therefore $Z_L = \infty$. This results in $\Gamma = 1$ and, with a trigonometric identity, equations E.12 become

$$V(z) = 2V_0^+[e^{-j\beta z} + e^{j\beta z}] = 2V_0^+ cos(\beta z) \tag{E.13a}$$

$$I(z) = \frac{V_0^+}{Z_0}[e^{-j\beta z} - e^{j\beta z}] = \frac{-2jV_0^+}{Z_0} sin(\beta z) \tag{E.13b}$$

The input impedance, given by

$$Z_{in} = \frac{V_z}{I_z} \tag{E.14}$$

is then equal to

$$Z_{in} = \frac{-jZ_0}{tan(\beta z)} \tag{E.15}$$

Because this thesis is analyzing a resonant system, the values for L and C used to determine β are the same that are used to find the resonant frequency of the device which is given by

$$\omega_0 = \frac{1}{\sqrt{LC}} \tag{E.16}$$

therefore equation E.8 becomes

$$\beta = \frac{\omega}{\omega_0} \tag{E.17}$$

and, since the device is operating at resonance, $\beta = 1$ and equation E.15 becomes

$$Z_{in} = \frac{-jZ_0}{tan(z)} \tag{E.18}$$

When the transmission line has a length $z = \frac{\lambda}{4} + \frac{n\lambda}{2}$ for any $n = 1, 2, 3, ...$ its impedance $z_{in} = 0$. Taken from chapter 3, figure E.3 shows the transmission line model as it applies to the active and inactive regions of the aluminum nitride CMR. The power delivered to

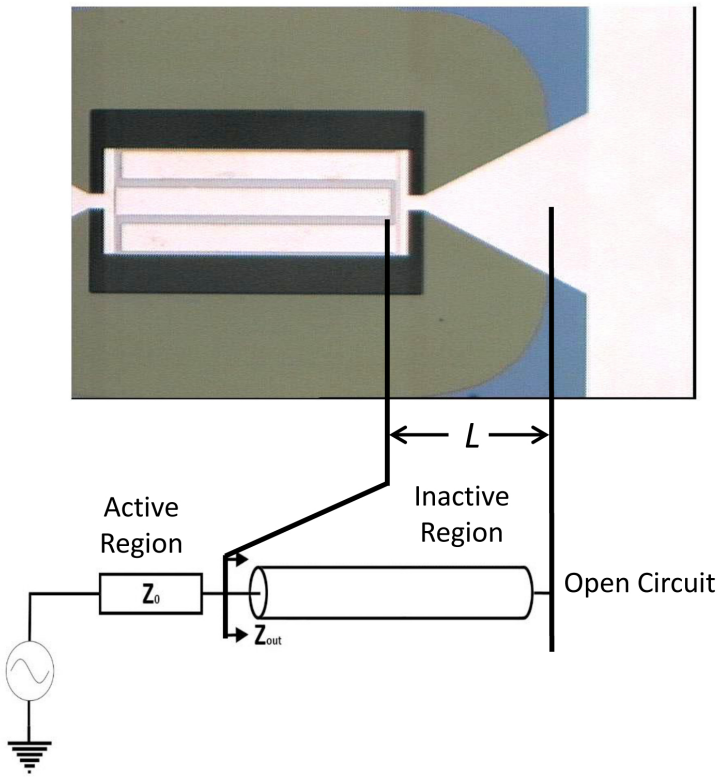

Figure E.3: The power dissipated to the anchor regions can be modeled as a transmission line with a characteristic impedance, Z_0.

the inactive region, P_{out} is given by

$$P_{out} = \frac{1}{2} Re(V_{in} I_{in}^*) = \frac{1}{2} |V_g|^2 | \frac{Z_{in}}{Z_{in} + Z_g} |^2 \tag{E.19}$$

where I_{in}^* is the complex conjugate of the current phasor at the edge of the active region, V_g is the voltage of the source and Z_{in} is the characteristic impedance of the inactive region as seen at the edge of the active region. Because the construction of the inactive region is identical to that of the active region the acoustic wave dissipation is similar for each and the value for Z_g, for our analysis, is equal to Z_0. Through simplification the power delivered to the inactive region becomes

$$P_{esc} = \text{abs}\left(V^2 \frac{\sin(2kL)}{4Z_0} \right) \tag{E.20}$$

where L is the length of the inactive region and k is the wavenumber.

Appendix F

Matlab Code for Finding Ring-Down Time Constant

```
clc
clear
clf
figure(gcf)

filename='c:\users\turnermems\Google Drive\DEFYS\Ringdown\NewData\220MHz\Al1p5um\Row2Col4\SinglePointRingDown';
% filename='d:\GoogleDrive\gibsoft\gibsoftv21\tempoutputfile.mat';
color=['r','g','b','y','k','c','m'];
SpatialPoint=1;
load(filename)
subplot(3,1,1);plot(-squeeze(Output.Delay(1,1,1,:))/1e-6,smooth(squeeze(Output.Displacement(1,SpatialPoint,1,:)),3)/1e-12,'.')
% ylim([0,1.1*max(Output.Displacement(1,1,1,:))]/1e-12)
hold on

Tau=3.3e-6;
TimeOffset=-1.5e-6;
Frequency=Parameters.FGN.FrequencySetting;
Q=pi*Tau*Frequency
SampleTime=Parameters.Vibrometer.SampleTime;
InitialMagnitude=75e-12;
ExpTimePoints=-squeeze(Output.Delay(1,1,1,:));
Fs=6e9;
NoiseFloor=0.1e-12;
```

```
24 RingDownLength=ExpTimePoints(end);
25 %% build analytical data
26 PreRollTime=linspace(2.5*ExpTimePoints(1),0,-Fs*(2.5*
       ExpTimePoints(1)));
27 PreRollSignal=(InitialMagnitude-NoiseFloor)*sin(Frequency*2*pi*
       PreRollTime)+NoiseFloor*sin(Frequency*2*pi*PreRollTime);
28 RingDownTime=linspace(0,ExpTimePoints(end)+3*SampleTime,Fs*(
       RingDownLength+3*SampleTime));
29 RingDown=(InitialMagnitude-NoiseFloor)*exp(-RingDownTime/Tau).*
       sin(Frequency*2*pi*RingDownTime)+NoiseFloor*sin(Frequency*2*
       pi*RingDownTime);
30 FullSignal=horzcat(PreRollSignal,RingDown);
31 FullSignalTime=horzcat(PreRollTime,RingDownTime)-TimeOffset;
32 %%
33 % Indexes=round(linspace(1,length(FullSignal),length(
       ExpTimePoints)));
34 for loop=1:length(ExpTimePoints)
35 Indexes(loop)=find(FullSignalTime>ExpTimePoints(loop),1);
36 end
37 Iteration = 1;
38 for loop=1:length(Indexes)
39     SampleWindow=FullSignal(Indexes(Iteration):Indexes(Iteration
           )+floor(SampleTime*Fs));
40     SampleWindowTime=FullSignalTime(Indexes(Iteration):Indexes(
           Iteration)+floor(SampleTime*Fs));
41
42     %% FFT
43     L = length(SampleWindow);
44     NFFT = 2^nextpow2(L);
45     Y = fft(SampleWindow,NFFT)/L;
46     f = Fs/2*linspace(0,1,NFFT/2+1);
47     mag=2*abs(Y(1:NFFT/2+1));
48     hold on
49     Peak(Iteration)=max(mag);
50     SimulationDelay(Iteration)=(SampleWindowTime(1));
51     Iteration = Iteration +1;
52 end
53 subplot(3,1,1);plot((SimulationDelay)/1e-6,Peak/1e-12,'r.')
54 subplot(3,1,2);plot(FullSignalTime,FullSignal)
55 subplot(3,1,3);plot(-squeeze(Output.Delay(1,1,1,:)),squeeze(
       Output.Voltage(1,1,1,:)))
```

Appendix G

Matlab Code for Finding Material Quality Factors

```
clc
clf
figure(gcf)
clear
%Lambda = 50.6um-AlN, 23.2um-Al, 12.7um-Pt
filename='d:\GoogleDrive\DEFYS\Ringdown\NewData\220MHz\Al1p5um\
    Row2Col2\BodyRingDown';
load(filename(1,:))
PeakPoint=31;% the point along the FFT that is sampled
Tau=1.95e-6;%Ring-Down time constant
TimeOffset=1.70e-6;%TIme Offset dialed into the FGN to allow a
    full ring-down
NoiseFloor=.1e-12;
InitialMagnitude=20.8e-12;
PlusPoints=3;
MinusPoints=3;
Frequency=Parameters.FGN.FrequencySetting;
Q=pi*Tau*Frequency
SampleTime=Parameters.Vibrometer.SampleTime;
ExpTimePoints=squeeze(Output.Delay(1,1,1,:));
ExpTimePoints=ExpTimePoints;
DelayPoints=squeeze(Output.Delay(1,1,1,:));
Fs=1/((norm(Parameters.SpatialPoints(end,:)-Parameters.
    SpatialPoints(1,:))*.3663e-6)/size(Parameters.SpatialPoints
    ,1));
L = length(Output.Displacement(1,:,1,1));
NFFT = 4*2^nextpow2(L);
```

```
24 %Create ring-down profile for experimental data
25 for DelayLoop=1:length(DelayPoints)%
26     Displacement=smooth(squeeze(Output.Displacement(1,:,1,
       DelayLoop)),3); %Build a mode shape for each delay time
27     %% Pull FFT
28     Y = fft(Displacement,NFFT)/L;%take a spatial FFT of that
       mode shape
29     f = Fs/2*linspace(0,1,NFFT/2+1);
30     Lambda=1./f;
31     mag=abs(Y(1:NFFT/2+1));
32     if (DelayLoop==2)
33         subplot(4,1,1);plot(smooth(squeeze(Output.Displacement
           (1,:,1,DelayLoop)),3)/1e-12)
34         subplot(4,1,2);plot(Lambda/1e-6,mag/1e-12)
35         hold on
36         plot(Lambda(PeakPoint)/1e-6,mag(PeakPoint)/1e-12,'r*')
37          xlim([0,70])
38     end
39     DecayCurve(DelayLoop)=max(mag(PeakPoint-MinusPoints:
       PeakPoint+PlusPoints));%Pull the magnitude of the desired
        peak
40 end
41 DecayCurve=smooth(DecayCurve,1)';
42 subplot(4,1,3);plot(-DelayPoints(1:DelayLoop)/1e-6,DecayCurve/1e
   -12,'.')
43 PeakWavelength=Lambda(PeakPoint)
44 %% fit curve
45 Fs=7e9;
46 RingDownLength=-ExpTimePoints(end);
47 %% build simulated data
48 PreRollTime=-linspace(ExpTimePoints(1)+TimeOffset,0,Fs*(
   ExpTimePoints(1)+TimeOffset));
49 PreRollSignal=(InitialMagnitude-NoiseFloor)*sin(Frequency*2*pi*
   PreRollTime)+NoiseFloor*sin(Frequency*2*pi*PreRollTime);
50 RingDownTime=linspace(0,-ExpTimePoints(end)+2*SampleTime,Fs*(
   RingDownLength+2*SampleTime));
51 RingDown=(InitialMagnitude-NoiseFloor)*exp(-RingDownTime/Tau).*
   sin(Frequency*2*pi*RingDownTime)+NoiseFloor*sin(Frequency*2*
   pi*RingDownTime);
52 FullSignal=horzcat(PreRollSignal,RingDown);
53 FullSignalTime=horzcat(PreRollTime,RingDownTime)+TimeOffset;
54 for loop=1:length(ExpTimePoints)
```

```
55 Indexes(loop)=find(FullSignalTime> -ExpTimePoints(loop),1);
56 end
57 Iteration = 1;
58 for loop=1:length(Indexes) %Repeat the procedure on the
       simulated data
59     SampleWindow=FullSignal(Indexes(Iteration):Indexes(Iteration
           )+floor(SampleTime*Fs));
60     SampleWindowTime=FullSignalTime(Indexes(Iteration):Indexes(
           Iteration)+floor(SampleTime*Fs));
61     %% FFT
62     L = length(SampleWindow);
63     NFFT = 2^nextpow2(L);
64     Y = fft(SampleWindow,NFFT)/L;
65     f = Fs/2*linspace(0,1,NFFT/2+1);
66     mag=2*abs(Y(1:NFFT/2+1));
67     hold on
68     Peak(Iteration)=max(mag);
69     SimulationTime(Iteration)=SampleWindowTime(1);
70     Iteration = Iteration +1;
71 end
72 subplot(4,1,3);plot((SimulationTime)/1e-6,Peak/1e-12,'r.')
73 subplot(4,1,4);plot(-DelayPoints,squeeze(Output.Voltage(1,1,1,:)
       ))
74 %% Create R^2 Value
75 YMean=mean(DecayCurve);
76 SSRes=sum((DecayCurve-Peak).^2);
77 SSTot=sum((DecayCurve-YMean).^2);
78 RSquared=1-(SSRes/SSTot)
```

Bibliography

[1] E. Suthers, *CTIA Annual Report*, 2016 (accessed June 3, 2016). `http://www.ctia.org/resource-library/press-releases/archive/americans-data-usage-more-than-doubled-in-2015`.

[2] E. Suthers, *2016 WiFi Shipments Exceed 15 Billion*.

[3] F. Nabki, K. Allidina, F. Ahmad, P. V. Cicek, and M. N. El-Gamal, *A highly integrated 1.8 ghz frequency synthesizer based on a mems resonator*, *IEEE Journal of Solid-State Circuits* **44** (Aug, 2009) 2154–2168.

[4] D. Moser, O. Brand, and H. Baltes, *A cmos compatible thermally excited silicon oxide beam resonator with aluminum mirror*, in *Solid-State Sensors and Actuators, 1991. Digest of Technical Papers, TRANSDUCERS '91., 1991 International Conference on*, pp. 547–550, June, 1991.

[5] J. S. Levy, A. Gondarenko, M. A. Foster, A. C. Turner-Foster, A. L. Gaeta, and M. Lipson, *Cmos-compatible multiple-wavelength oscillator for on-chip optical interconnects*, *Nature Photonics* **4** (2010), no. 1 37–40.

[6] C. Zuo, J. Van der Spiegel, and G. Piazza, *1.05-ghz cmos oscillator based on lateral-field-excited piezoelectric aln contour-mode mems resonators*, *Ultrasonics, Ferroelectrics, and Frequency Control, IEEE Transactions on* **57** (2010), no. 1 82–87.

[7] Z. Hao and B. Liao, *An analytical study on interfacial dissipation in piezoelectric rectangular block resonators with in-plane longitudinal-mode vibrations*, *Sensors and Actuators A: Physical* **163** (2010), no. 1 401–409.

[8] R. H. Olsson, J. G. Fleming, K. E. Wojciechowski, M. S. Baker, and M. R. Tuck, *Post-cmos compatible aluminum nitride mems filters and resonant sensors*, in *2007 IEEE International Frequency Control Symposium Joint with the 21st European Frequency and Time Forum*, pp. 412–419.

[9] G. Piazza, P. J. Stephanou, and A. P. Pisano, *Piezoelectric aluminum nitride vibrating contour-mode MEMS resonators*, *Journal of Microelectromechanical Systems* **15** (2006), no. 6 1406–1418.

[10] R. Ruby, P. Bradley, J. D. Larson, and Y. Oshmyansky, *Pcs 1900 mhz duplexer using thin film bulk acoustic resonators (fbars)*, *Electronics Letters* **35** (May, 1999) 794–795.

[11] K. E. Wojciechowski, B. E. Boser, and A. P. Pisano, *A mems resonant strain sensor operated in air*, in *Micro Electro Mechanical Systems, 2004. 17th IEEE International Conference on. (MEMS)*, pp. 841–845, 2004.

[12] C. T. Nguyen, *High-q micromechanical oscillators and filters for communications*, in *Circuits and Systems, 1997. ISCAS'97., Proceedings of 1997 IEEE International Symposium on*, vol. 4, pp. 2825–2828, 1997.

[13] A. Prasad, J. Charmet, and A. A. Seshia, *Simultaneous interrogation of high-q modes in a piezoelectric-on-silicon micromechanical resonator*, *Sensors and Actuators A: Physical* **238** (2016) 207–214.

[14] J. Segovia-Fernandez and G. Piazza, *Analytical and numerical methods to model anchor losses in 65-mhz aln contour mode resonators*, *Journal of Microelectromechanical Systems* **25** (June, 2016) 459–468.

[15] T. H. Lee and A. Hajimiri, *Oscillator phase noise: a tutorial*, *IEEE Journal of Solid-State Circuits* **35** (March, 2000) 326–336.

[16] G. G. Yaralioglu, A. S. Ergun, B. Bayram, E. Haeggstrom, and B. T. Khuri-Yakub, *Calculation and measurement of electromechanical coupling coefficient of capacitive micromachined ultrasonic transducers*, *IEEE transactions on ultrasonics, ferroelectrics, and frequency control* **50** (2003), no. 4 449–456.

[17] C. Cassella, Z. Qian, G. Hummel, and M. Rinaldi, *1.02 ghz cross-sectional lamb mode resonator with high k_t^2 exceeding 4.6%*, in *2016 IEEE 29th International Conference on Micro Electro Mechanical Systems (MEMS)*, pp. 659–662, Jan, 2016.

[18] M. Cremonesi, A. Frangi, C. Cassella, and G. Piazza, *Enhancement of the quality factor of AlN contour mode resonators by acoustic reflection: Numerical design and experimental investigation*, *Procedia Engineering* **87** (2014) 468–471.

[19] J. Segovia-Fernandez, M. Cremonesi, C. Cassella, A. Frangi, and G. Piazza, *Experimental study on the impact of anchor losses on the quality factor of contour mode AlN resonators*, in *Solid-State Sensors, Actuators and Microsystems (TRANSDUCERS EUROSENSORS XXVII), 2013 Transducers Eurosensors XXVII: The 17th International Conference on*, pp. 2473–2476, June, 2013.

[20] R. C. Ruby, P. Bradley, Y. Oshmyansky, A. Chien, and J. D. Larson III, *Thin film bulk wave acoustic resonators (fbar) for wireless applications*, in *Ultrasonics Symposium, 2001 IEEE*, vol. 1, pp. 813–821, IEEE, 2001.

[21] M.-A. Dubois and P. Muralt, *Stress and piezoelectric properties of aluminum nitride thin films deposited onto metal electrodes by pulsed direct current reactive sputtering*, *Journal of Applied Physics* **89** (2001), no. 11 6389–6395.

[22] C. Cassella and G. Piazza, *Aln two-dimensional-mode resonators for ultra-high frequency applications*, *IEEE Electron Device Letters* **36** (2015), no. 11 1192–1194.

[23] G. D. Cole, I. Wilson-Rae, K. Werbach, M. R. Vanner, and M. Aspelmeyer, *Phonon-tunnelling dissipation in mechanical resonators*, *Nature communications* **2** (2011) 231.

[24] D. Binder, E. Quevy, T. Koyama, S. Govindjee, J. W. Demmel, and R. T. Howe, *Anchor loss simulation in resonators*, in *Micro Electro Mechanical Systems, 2005. MEMS 2005. 18th IEEE International Conference on*, pp. 133–136, IEEE.

[25] A. Bijari, S.-H. Keshmiri, and F. Babazadeh, *Nonlinear modeling for distortion analysis in silicon bulk-mode ring resonators*, *Micromachines* **3** (2012) 582–603.

[26] Y.-H. Park and K. C. Park, *High-fidelity modeling of mems resonators. part i. anchor loss mechanisms through substrate*, *Journal of Microelectromechanical Systems* **13** (April, 2004) 238–247.

[27] U. Basu and A. K. Chopra, *Perfectly matched layers for time-harmonic elastodynamics of unbounded domains: theory and finite-element implementation*, *Computer methods in applied mechanics and engineering* **192** (2003), no. 11 1337–1375.

[28] D. Binder, E. Quevy, T. Koyama, S. Govindjee, J. Demmel, and R. Howe, *Anchor loss simulation in resonators*, in *Micro Electro Mechanical Systems, 2005. MEMS 2005. 18th IEEE International Conference on*, pp. 133–136, Jan, 2005.

[29] J.-P. Berenger, *A perfectly matched layer for the absorption of electromagnetic waves*, *Journal of computational physics* **114** (1994), no. 2 185–200.

[30] J. Segovia-Fernandez and G. Piazza, *Analytical and numerical methods to model anchor losses in 65-mhz aln contour mode resonators*, *Journal of Microelectromechanical Systems* **25** (2016), no. 3 459–468.

[31] Z. Hao and B. Liao, *An analytical study on interfacial dissipation in piezoelectric rectangular block resonators with in-plane longitudinal-mode vibrations*, *Sensors and Actuators A: Physical* **163** (2010), no. 1 401–409.

[32] J. Segovia-Fernandez and G. Piazza, *Damping in 1 ghz laterally-vibrating composite piezoelectric resonators*, in *Micro Electro Mechanical Systems (MEMS), 2015 28th IEEE International Conference on*, pp. 1000–1003, IEEE.

[33] J. F. Vignola, J. A. Judge, J. Jarzynski, M. Zalalutdinov, B. H. Houston, and J. W. Baldwin, *Effect of viscous loss on mechanical resonators designed for mass detection*, *Applied Physics Letters* **88** (2006), no. 4 041921.

[34] L. Shi and G. Piazza, *Investigations on quality factor of high frequency laterally vibrating ln on sio 2 microresonators*, in *Ultrasonics Symposium (IUS), 2014 IEEE International*, pp. 578–581, IEEE.

[35] C. Zuniga, M. Rinaldi, and G. Piazza, *Reduced viscous damping in high frequency piezoelectric resonant nanochannels for sensing in fluids*, in *Micro Electro Mechanical Systems (MEMS), 2011 IEEE 24th International Conference on*, pp. 960–963, Jan, 2011.

[36] B. Antkowiak, J. Gorman, M. Varghese, D. Carter, and A. Duwel, *Design of a high-q, low-impedance, ghz-range piezoelectric mems resonator*, in *TRANSDUCERS, Solid-State Sensors, Actuators and Microsystems, 12th International Conference on, 2003*, vol. 1, pp. 841–846, IEEE.

[37] R. Lifshitz and M. L. Roukes, *Thermoelastic damping in micro-and nanomechanical systems*, *Physical review B* **61** (2000), no. 8 5600.

[38] Z. Hao, Y. Xu, and S. K. Durgam, *A thermal-energy method for calculating thermoelastic damping in micromechanical resonators*, *Journal of Sound and Vibration* **322** (2009), no. 4 870–882.

[39] K. Y. Yasumura, T. D. Stowe, E. M. Chow, T. Pfafman, T. W. Kenny, B. C. Stipe, and D. Rugar, *Quality factors in micron-and submicron-thick cantilevers*, *Microelectromechanical Systems, Journal of* **9** (2000), no. 1 117–125.

[40] M. Giovannini, S. Yazici, N.-K. Kuo, and G. Piazza, *Spurious mode suppression via apodization for 1 GHz AlN contour-mode resonators*, in *Frequency Control Symposium (FCS), 2012 IEEE International*, pp. 1–5, IEEE, 2012.

[41] G. Piazza, P. J. Stephanou, and A. P. Pisano, *One and two port piezoelectric higher order contour-mode MEMS resonators for mechanical signal processing*, *Solid-State Electronics* **51** (2007), no. 1112 1596 – 1608. Special Issue: Papers Selected from the 36th European Solid-State Device Research Conference - ESSDERC06.

[42] C. Cassella, J. Segovia-Fernandez, and G. Piazza, *Segmented electrode excitation of AlN contour mode resonators to optimize the device figure of merit*, in *IEEE Transducers*, 2013.

[43] D. S. Bindel and S. Govindjee, *Elastic pmls for resonator anchor loss simulation*, *International Journal for Numerical Methods in Engineering* **64** (2005), no. 6 789–818.

[44] C. Cassella, S. Navab, B. W. Soon, and G. Piazza, *Quality factor dependence on the inactive regions in AlN contour-mode resonators*, *Journal of Microelectromechanical Systems* (2015) to be published.

[45] B. Harrington and R. Abdolvand, *In-plane acoustic reflectors for reducing effective anchor loss in lateral extensional mems resonators*, *Journal of Micromechanics and Microengineering* **21** (2011), no. 8 085021.

[46] A. Klempner, R. Marinis, P. Hefti, and R. Pryputniewicz, *Experimental determination of the q-factors of microcantilevers coated with thin metal films*, *Strain* **45** (2009), no. 3 295–300.

[47] C. Rembe, G. Siegmund, H. Steger, and M. Wörtge, *Measuring mems in motion by laser-doppler vibrometry*, *Optical Inspection of Microsystems* (2006) 245–292.

[48] T. Hiller, L. L. Li, E. L. Holthoff, B. Bamieh, and K. L. Turner, *System identification, design, and implementation of amplitude feedback control on a nonlinear parametric mem resonator for trace nerve agent sensing*, *Microelectromechanical Systems, Journal of* **24** (2015), no. 5 1275–1284.

[49] A. Frangi, M. Cremonesi, A. Jaakkola, and T. Pensala, *Analysis of anchor and interface losses in piezoelectric MEMS resonators*, *Sensors and Actuators A: Physical* **190** (2013), no. 0 127 – 135.

[50] Y. Yeh and H. Cummins, *Localized fluid flow measurements with an hene laser spectrometer*, *Applied Physics Letters* **4** (1964), no. 10 176–178.

[51] F. Eberhardt and F. Andrews, *Laser heterodyne system for measurement and analysis of vibration*, *the Journal of the Acoustical Society of America* **48** (1970), no. 3A 603–609.

[52] C. Rembe, S. Boedecker, A. Drbenstedt, F. Pudewills, and G. Siegmund, *Heterodyne laser-doppler vibrometer with a slow-shear-mode bragg cell for vibration measurements up to 1.2 ghz*, in *Proc. SPIE*, vol. 7098, p. 70980A.

[53] S. Heinrich, W. Michael, S. Georg, and R. Christian, *Measuring MEMS in Motion by Laser Doppler Vibrometry*, pp. 245–292. Optical Science and Engineering. CRC Press, 2006.

[54] G. Gonzalez, *Foundations of oscillator circuit design*. Artech House, 2007.

[55] A. Hajimiri and T. H. Lee, *A general theory of phase noise in electrical oscillators*, *IEEE journal of solid-state circuits* **33** (1998), no. 2 179–194.

[56] R. Cerda, *Sources of phase noise and jitter in oscillators*, *Mpdigest feature article* (2006) 1–2.

[57] D. B. Leeson, *A simple model of feedback oscillator noise spectrum*, *Proceedings of the IEEE* **54** (1966), no. 2 329–330.

[58] J. D. Larson III, P. D. Bradley, S. Wartenberg, and R. C. Ruby, *Modified butterworth-van dyke circuit for fbar resonators and automated measurement system*, in *Ultrasonics Symposium, 2000 IEEE*, vol. 1, pp. 863–868, IEEE, 2000.

[59] M. P. David, *Microwave and rf design of wireless systems*, 2000.